Quantitative hybrid modeling reveals predictable mechanical stress response of growing tumor spheroids

P. Van Liedekerke[a,*], J. Neitsch[b], T. Johann[b], K. Alessandri[c], P. Nassoy[c], D. Drasdo[a,b,*]

[a] *INRIA de Paris and Sorbonne Universits UPMC Univ Paris 6, LJLL, France*
[b] *IZBI, University of Leipzig, Leipzig, Germany*
[c] *Institut Optique, Talence , France*

Abstract

By a hybrid computational modeling strategy we demonstrate that the growth response of tumors under mechanical stress may be quantitatively predictable even under largely differing growth conditions. In our computational models, cells are represented by individual units parameterized by measurable biophysical and cell-biological parameters. We assume a simple functional relation how cell cycle progression is controlled by volumetric strain, the latter in our model being derived from a biomechanical relation between applied pressure and cell compressibility. After parameter calibration from experiments with CT26 cells growing against resistance of a thin elastic alginate capsule, the model adequately predicts both the growth curve in thick capsules and, after accounting for differences in the growth conditions, in a Dextran solution experiment, where the stress is generated by osmosis. Our modeling strategy is very general, and provides an important technical achievement for dealing with high compression in individual-based models that enjoy increasing interest.

1. Introduction

Mechanotransduction, or the mechanism by which cells transform an external mechanical stimulus into internal signals emerges in many cellular processes, such as embryonal development and tumor growth [1]. Cell growth in a confined environment such as stroma increases cell density and affects the balance between tissue growth in homeostasis [2, 3]. In their papers, Helmlinger et al. (1997) and later Cheng et al. (2009) and Mills et al. (2014) [4, 5, 6] experimentally investigated the growth of spheroids embedded in agarose gel at varying agarose concentration. Spheroids under pressure were also studied using the osmotic effects induced by Dextran concentrations [7]. Recent findings suggest that this stagnation of growth is due to a volume decrease of the cells [8]. In all cases it was found that mechanical stress affects spheroid growth inhibitory, yet a quantitative relation between pressure and cell fate and is far less conclusive.

Here we in a first step establish a computational model to quantitatively explain the growth kinetics and multicellular pattern found for CT26 (mouse colon carcinoma cell line) multicellular spheroids constrained by a spherical elastic capsule with defined properties. Once the spheroid touches the capsule, further radial expansion depends on the pressure exerted by the cell aggregate. This novel experimental technique, called the "Cellular Capsule Technology" [9], has opened a new possibility to study growth of tumor multicellular spheroids in a mechanically controlled way. The spheroids are monitored during a period of several days. Histological data of the spheroids are collected and analyzed using staining, cryosections and microscopy. In addition, the experiment has been conducted on capsules with varying thickness to mimic the mechanical resistance of the environment. We refer to this experimental technique as "Experiment I".

Delarue et. al. (2014) [8] demonstrated the effect of mechanical stress on multicellular growth using the same cell line in a different experimental setting. This gives the opportunity to study in a second

*Corresponding authors
Email addresses: paul.van_liedekerke@inria.fr (P. Van Liedekerke), Dirk.Drasdo@inria.fr (D. Drasdo)

step, how far the computational model established to explain experiment I, would have to be modified to quantitatively explain this experiment (referred to as "experiment II" from now on). In experiment II mechanical compression was imposed using the osmotic effects induced by a Dextran solution. The main difference between those two experiments is that in the first experiment pressure gradually increases with increasing deformation of the elastic capsule, while in the second, a constant pressure (5 kPa) is maintained. Furthermore, in the second case there is no obstructing tissue present (see Fig. 1a, respectively Exp. I and Exp. II).

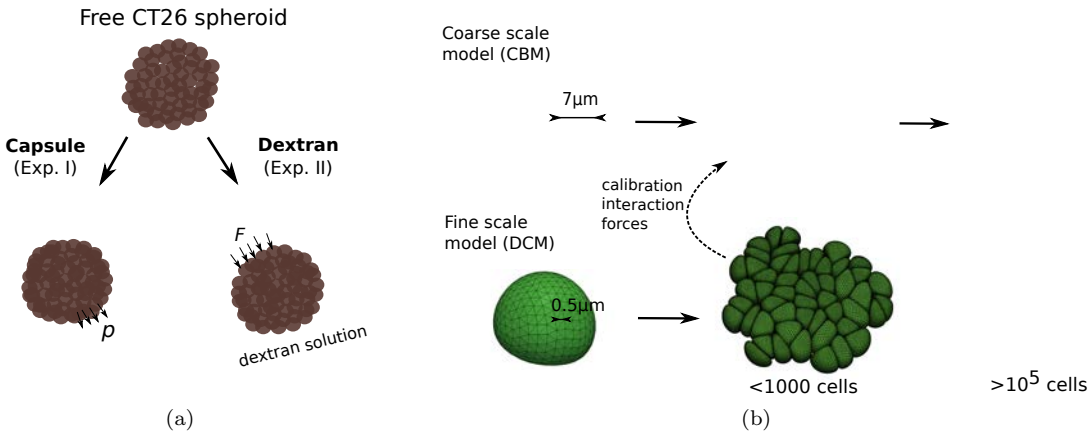

Figure 1: (a) Two experiments setups for growing spheroids (free and mechanically stressed) considered in our model. (b) Multi-scale modeling approach, considering two model scales where the parameters from the coarse scale are determined for runs with the fine scale model.

As modeling technique we developed an Agent Based Model (ABM) that is parameterized by biophysical and cell-kinetic parameters. Different from continuum models which consider locally averaged variables (such as cell density, momentum density, ...) [10, 11] agent based models represent each cell individually hence allow to account for cell to cell variability and inhomogeneities on small spatial scales, and tie measurable quantities at the cell level to the emergent behavior at the multicellular level. Simulations with center based models (CBM), a prominent representative in the class of ABMs where forces between cells are calculated as forces between cell centers, indicated the necessity of mechanical growth inhibition in monolayer growth [13]. The same model type was able to quantitatively reproduce the experimentally observed growth kinetics of monolayers, as well as of multicellular spheroids growing in liquid suspension [14, 15, 16] and embedded in agarose gel [17] if cell cycle progression was assumed to be inhibited either as a consequence of pressure or of a too small distance of the cell centers. However, as no information about the mechanical stresses was available for the underlying experiments, a quantitative coupling between mechanical pressure and growth inhibition was not feasible. Cell populations subject to large compression forces represent an unresolved technical challenge to the current generation of ABMs [18] which is why we here develop a sophisticated two-level modeling strategy where the parameters of the CBM which considers the cell shape in a statistical, "coarse grained" sense thereby permitting simulations of large cell population sizes, are calibrated from a finer scale cell model "DCM", that displays cell shape at high resolution at the expense of high computational cost (see Fig. 1b). As both CBM and DCM are parameterized by measurable quantities, the possible parameter range of each model parameter can be identified and un-physiological parameter choices can be avoided.

To unravel the multicellular dynamics with the model, our modeling strategy is to postulate and implement hypotheses on cell growth, quiescence and death, and iteratively adapt or extend them in case the model simulations are falsified by comparison with the experimental data. Pursuing the same strategy allowed predictions of subsequently validated mechanisms in liver regeneration [19, 20]. Based upon analysis of the relation between pressure, cell density and cell compressibility, our findings suggest that contact

inhibition can be regarded as a continuous process imposed by a reduction of cell volume as a consequence of increasing pressure and individual cell compressibility. In addition, the high resolution model shows that potential effects of micro mechanics at the interfaces with the capsule may depend on the mechanical properties of the cells.

Experiment I

Small clumps of CT26 cells were grown in a humidified atmosphere to to reach a radius of about $100\,\mu$m (see [9] for details). When the tumor cells reached the border of the elastic alginate capsule ($t = 0d$ in Fig. 2a), they induce a dilatation of the radius, which is an indicator of the pressure they exert. The capsule expansion was measured from the point of confluence on and its radius was monitored during several days, while histological data of the spheroids were collected at the point of confluence and at $48h$ after. The capsules had an initial radius of $\pm 100\,\mu$m. Two capsule thicknesses have been studied to mimic a variation in mechanical resistance. In unraveling the mechanisms of growing cells under confinement, we first extract three principal observations in the experiments:

(E1.OI) In the absence of a capsule, an initial exponential growth phase was observed with doubling time $T_{div} = 17h$ up to $R > 100\,\mu$m [9]. Two days after confluence, the growth kinetics starts to deviate clearly from exponential growth ($R \approx 175\,\mu$m), see Fig. 2a. (E1.OII) At confluence, the time evolution of the capsule radius shows an initial growth stage T_1 ($t < 1d$, $\sim 8\,\mu$m/d for a thin capsule) followed by slower quasi-linear residual growth stage T_2 ($t > 1d$) that at least persists for several days. The observed growth velocities were $\sim 2\,\mu$m/d for the thin capsules (Fig. 2a) and $0.7\,\mu$m/d for the thick capsules (Fig. 7). (E1.OIII) The nuclei density, obtained from cryosections, increases from $\sim$1 nucleus / $100\,\mu\text{m}^2$ before confinement, to roughly 2 nuclei / $100\,\mu\text{m}^2$ at $48h$ after confluence, with a relatively higher number near the center of the spheroid (1.2 times more compared to the outer regions), and local increase right at the border of the capsule. (E1.OIV) Most of the cells in the bulk are necrotic after $48h$ of confinement. However, the cells in the periphery, corresponding to roughly 2 cell layers ($15\,\mu$m), stay mostly viable during the time course T_2 of the experiment. The distribution of cell nuclei in Alessandri et al. (2013) suggests that cells near the capsule border are deformed while those in the interior look isotropically shaped.

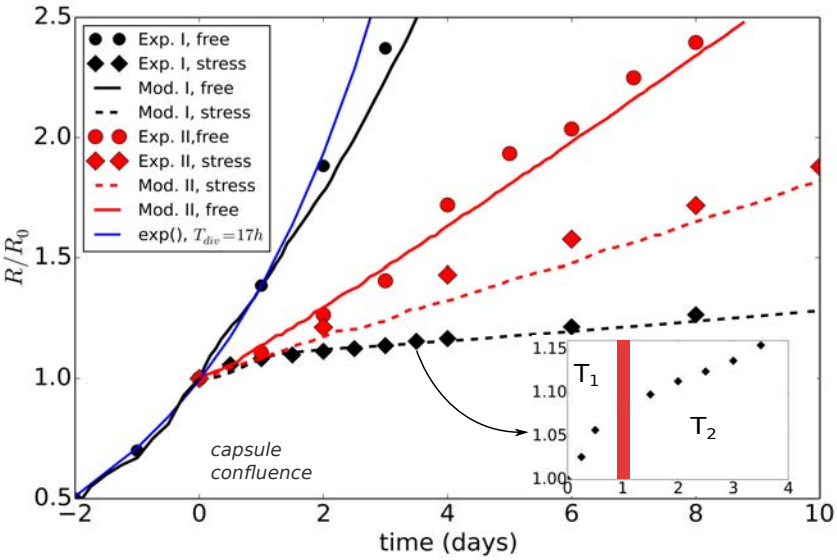

(a)

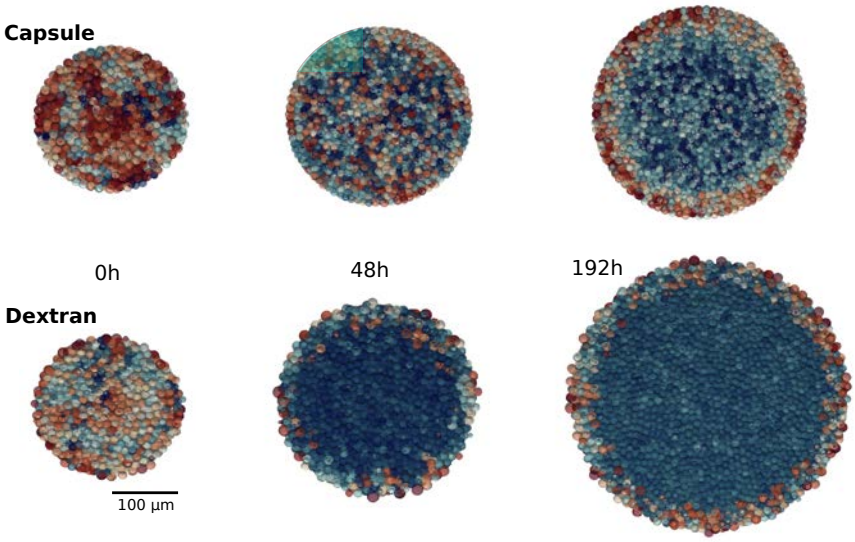

(b)

Figure 2: (a) Radial growth curves data of the spheroids for experiment I and II and respective model runs ($R_0 = 100\,\mu$m). The model runs with growth rate adaption (Model Ib) are indicated by dashed or full lines. The thin blue line indicates pure exponential growth with doubling time of $17h$. For clarity, the model run without growth rate adaption (Model 0) is not shown, but matches very well with the exponential. (b) Agent Based Model simulation time sequence for experiment I and II respectively. The color coding is according to their size (red is bigger, dark blue is smaller).

Experiment II

In the work of Delarue et al. (2014) [8], CT26 spheroids (initial radius $100\,\mu$m) were grown in a Dextran solution, which expels the water out of the spheroid and generates osmotic forces exerted to the outer cells which then are transferred as compressive stresses to the interior (the bulk) cells. The concentration of

Dextran regulates the applied pressure. (E2.OI) The growth rate at $p = 5\,\text{kPa}$ is significantly lower than in control spheroids where no pressure is exerted. (E2.OII) Surprisingly, the spheroid free growth data do not show an initial exponential phase found in (E1.OI) ($T_{div} = 17h$) (Fig. 2a). This discrepancy might be explained by the different culturing conditions in both experiments. During the stress conditions, no significant changes in apoptosis rates after 3 days, yet over-expression of the kinase inhibitor $p27^{Kip1}$ with an increased number of cells arrested in the G1 phase were observed.

2. Results

2.1. Hypotheses for growth and death of tumor cells

In order to explain the experimental growth patterns in both experiments (1, 2) with a mathematical model, we propose a number of hypotheses for the growth dynamics in relation to stress that should apply to both experiments. The hypotheses are stepwise implemented in the model to identify those necessary to explain the observations. In the later sections the general hypotheses are complemented by model assumptions that take into account specific features of each individual experiment.

(H.I) In both experiments sub-exponential growth is observed, in EI.OIV the formation of a necrotic core. We assume that deviation of growth from an exponential indicates limitation of proliferation to a proliferating rim. Interior cells can undergo necrosis as a consequence of a lack of nutriments or other factors [14, 21]. This may indirectly be promoted by pressure, e.g., if the cell layer below the capsule is so much compressed that it forms an obstructive barrier for some nutriments (as glucose) for cells located further in the interior of the tumor. However, cell death may also be a direct consequence of mechanical pressure e.g., if cells subject to compression cannot advance in cell cycle for too long and then undergo apoptosis. We do not specify the reason for cell death here but define the thickness of the proliferating rim by the parameter λ_{crit}. Necrotic cells can undergo lysis, in which they steadily lose a part of their fluid mass. The decrease of mass is limited to about 70% of the total initial mass of the cell [22].

(H.II) Cell growth rate maybe be declined or inhibited by pressure [14, 4]. The authors of a recent study [8] hypothesized that the growth rate may be down-regulated if the cell volume is reduced as a consequence of pressure. On the molecular level, volume reduction correlates with over expression of $p27^{Kip1}$ (a protein which inhibits cell proliferation) which progressively decreases the proliferating potential. These observations suggest that quiescence, and perhaps also apoptosis may thus be controlled by either pressure or cell volume. Experimental studies [23, 24, 25, 26] mainly measured the growth rate of dry mass or size. These indicate that the growth rate (α) varies within the cell-cycle, yet a unique relationship is difficult to infer. Here we assume 1) that the growth of the cell population not constrained by mechanically-induced growth inhibition, nutrient, oxygen or growth factor limitations is exponential, and 2) that the volume growth rate is constrained if cells are exposed to compressive stress. We assume that growth rate is dependent on the volumetric strain ("true strain", commonly used in case of large strains) $\epsilon_V = -\log(V/V_{ref})$ where V is the actual compressed volume and V_{ref} is the volume of the cell in free suspension. The degree to which a cell upon volumetric compression changes its volume can be described by its compression modulus K. The compression modulus of the cell depends on the actual volume fraction of water, and the elastic response of the cytoskeleton structure and organelles. It may also be influenced by the permeability of the plasma membrane for water, the presence of caveolae [27], and active responses in the cells. As such, the timescale at which K is measured is important. In our simulations, we regard K as the long timescale modulus of cell, as growth and divisions are slow processes. The calculation of growth, volume and pressure for each cell in the model is explained in the *Methods* section).

We propose as general form for growth rate α the Hill formula:

$$\alpha = \alpha_0 \frac{\epsilon_{V_{tr}}^n}{\epsilon_V^n + \epsilon_{V_{tr}}^n}, \tag{1}$$

where α_0 is the growth rate of the unconstrained cell, $\epsilon_{V_{tr}}$ is a threshold value[1], and n is an integer. The parameter $\epsilon_{V_{tr}}$ is the value where the cells have lost 50% of their initial growth rate (see Fig. 3a). Note

[1] We assume $V/V_{ref} \leq 1$ in the experiment meaning the the cells are always in a compressive state

that for $\epsilon_{V_{tr}} \to \infty$ we retrieve a constant growth scenario, whereas if $n \to \infty$ a sharp pressure threshold is recovered. This makes a variety of growth scenarios possible. Hill formulas have been used in the past to simulate contact inhibition in epithelial tissue and tumors [28, 16, 29].

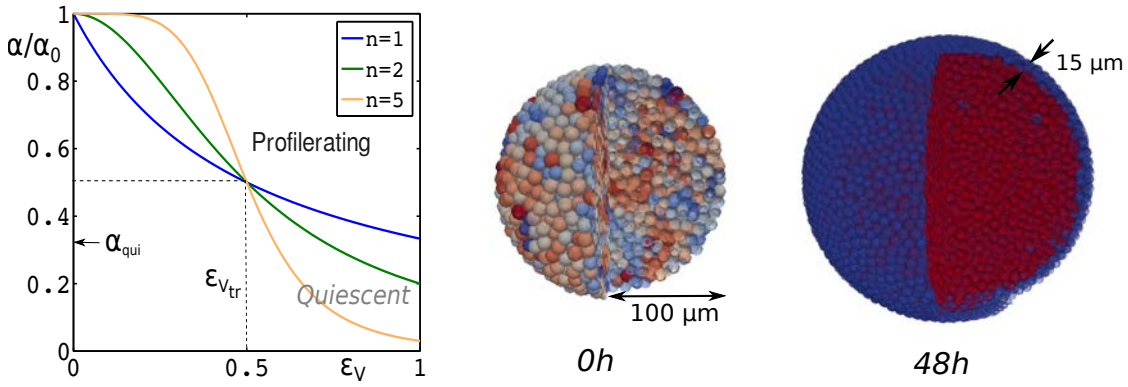

(a) (b)

Figure 3: (top) (a) Proposed function for the growth rate for different values of n with indication of α_{qui} for which below the growth stalls. (b) Left: simulation of a CT26 spheroid just before confinement (coloring according to cell volume), right: after $48h$ of confinement in capsule (coloring indicate necrotic cells (red) and viable cells (blue).

(H.III) It is generally accepted that cells who have passed the G1 checkpoint (also known as restriction point) are committed to divide. In our model we assume this checkpoint is situated after 1/4 of the total cell cycle time [30]. The transition to the quiescence state of a cell can be defined as the one at which the growth rate "stalls", i.e. $\alpha/\alpha_0 < \alpha_{qui}$ (see Fig. 3a).

2.2. Establishment of the model

We used an agent based model of the center based type to mimic the multicellular growth. In this model each cell is represented individually and parameterized by measurable biophysical and bio-kinetic parameters. This facilitates determination of the parameter ranges and thereby a sensitivity analysis [19]. Cell movement is modelled by an equation of motion, that balances friction with compression, adhesion, micro motility forces, as well as external forces (e.g. capsule) exerted on that cell. A Center Based Model (CBM) approximates each cell as inherently spherical object that deforms moderately upon compression (see *Methods* section). Forces between cells are transmitted as forces between the cell centers. CBMs permit realistic simulations as they directly use physical forces. They are amenable to about 1 Mio cells in two weeks computation time on a standard desktop computer. However, basic CBMs generally lack a self-consistent definition cell volume, shape and mechanical stresses on the cell [18] which provides a critical limitation here for simulating cells subject to large compressive stress. This can be circumvented by using deformable cell models (DCMs) instead of CBMs. In this model type, each cell surface is triangulated and the deformations and stresses can be tracked precisely. However, a DCM simulation is computationally very expensive. To permit simulations of large cell populations in reasonable time, while ensuring a realistic behavior at high compression, we therefore use a hybrid modeling strategy in which we calibrate the interaction forces of the CBM with numerical experiments using the DCM, and then use the modified CBM to simulated the compression Experiments 1 and 2 *in silico* (for details, see *Methods*, section 4.3). A conceptually related idea has been pursued in refs. [31, 12, 32], where an agent based model and continuum model have been combined to achieve simulations of larger tumors without losing the necessary detail in the proliferating rim.

According to hypothesis H.II growth rate depends on the compression of the cells, hence the volume doubling time can locally vary and is larger than for uncompressed cells. Limiting cases would be that

division occurred after volume doubling at a variable time [14], or after a pre-defined time [20]. We therefore also compared the effect of constant time vs. doubling of volume criterion in cell division on the cell population behavior. The execution order of the model components is depicted in Fig. 14. Also mentioned in H.II, the growth rate may vary during the cell cycle. To study the effect of a varying growth rate we ran all simulations with constant growth rate, as well as exponential growth rate during the cell cycle (details in *Methods* section 4.1.5).

2.3. Simulation of experiment I for thin capsules: constant growth rate

In this section we consider a constant growth rate, assuming first a constant compression modulus, then strain hardening, and finally including volume shrinkage due to lysis.

"Model 0": First, we simulated CT26 cells growing freely in the liquid suspension, hereafter referred to as "Model 0" (for the parameters, see Table 1). For a constant cell cycle duration of $T_{div} = 17h$ (no inhibition), in the observation period $-2\,\mathrm{d} \leq t \leq 1\,\mathrm{d}$, we found a good mutual agreement between the model, the experimental growth curve, and an exponential, see Fig. 2a. This determines the intrinsic cell cycle duration T_{div} of a growing cell population subject to neither external mechanical stress nor nutriment limitation. The results in "Model 0" are hardly affected by the cell compressibility. A movie (Video 1) of this simulation is provided in the *Supplementary material*.

In the next step, we used the same model to mimic a growing multicellular spheroid in a thin capsule ($H = 8\,\mu\mathrm{m}$). Until confluence ($t = 0$) is reached, the radial growth curve in the experiment is close to that of a spheroid growing in liquid suspension indicating that the presence of the capsule has no notable influence on the growth of the spheroid. However at confluence, the growth curve exhibits a decline followed by rather a sharp transition into an approximately linear slope ($t \leq 1d$ and $t \geq 1d$ respectively in Fig. 2a). As we do not explicitly model nutriment influences which would require a lot of experiments at varying nutriment conditions displaying proliferating and viable cells as necrotic lesions [21], we capture the effect by introducing a critical distance from the capsule, $\lambda_{crit} = 15\mu m$, over which cells remain viable during linear stage (see E1.OIV and H1). The transition for the cells from T_1 to T_2 is modeled by introducing a critical pressure p_{crit} in the capsule (see *Methods* section 4.4). At this pressure, the cells in the bulk of the spheroid start to die, while the ones at the border remain viable.

"Model Ia": The compression modulus of the cells influences the volumetric strain and thus growth rate. In "Model Ia" we varied K in the range $K \in [2500\,\mathrm{Pa}, 150\,\mathrm{kPa}]$, which includes the value of $K \approx 10kPa$ reported for CT26 cell [8, 33, 34]. In Fig. 4a we compare the radius of the capsule upon deformation by the growing multicellular spheroid with the experiment. Note that all simulations exhibit a short initial lag, in where the capsule dilatation is small. In this stage, the spheroid touches the capsule border but cells are mainly pushed inwards, filling up intercellular spaces. This is less visible in the experiment, yet there the exact point of confluence is very difficult to determine. After this period, cells are becoming more and more compressed and the mechanical resistance of the spheroid increases. Fig. 4b further also shows the simulated and experimentally observed nuclei densities.

For $K = 10\,\mathrm{kPa}$ both the initial and the residual radial growth are significantly overestimated. Moreover, the cell density increases at $48h$ only by a factor of 1.5, while experimentally a factor of 2 is observed (Fig. 4). This suggests that the apparent compressibility of the spheroid is too high, supported by observing that at $K = 150\,\mathrm{kPa}$ the initial radial growth becomes much too high whereas the cell density at $48h$ is now only 1.3 times the original one (Fig. 4b). Contrary, for a much smaller value $K \sim 2500\,\mathrm{Pa}$ as deduced in [35], the initial and residual growth curves are closer to the experiment but still to high. Moreover, while for the compression moduli $K = 10\,\mathrm{kPa}, 150\,\mathrm{kPa}$, the radius expansion was linear, it bends now upwards for $K = 2500\,\mathrm{Pa}$, as more and more cells reach the maximum limit of fluid expel (H.I) and cause a stiff response of the spheroid system as we do not allow further compression in the model. More importantly, we now observe a far too high cell density at $48h$ (increase of almost 3 times). These results demonstrate that the proliferating rim with $\lambda_{crit} = 15\mu m$ alone cannot not explain the velocity of the growing spheroid in the linear phase, as it is not possible to simultaneously fit the nuclei density and the long-time radius expansion. For any value that would be capable of fitting the nuclei density, the slope of the radius expansion would be too high.

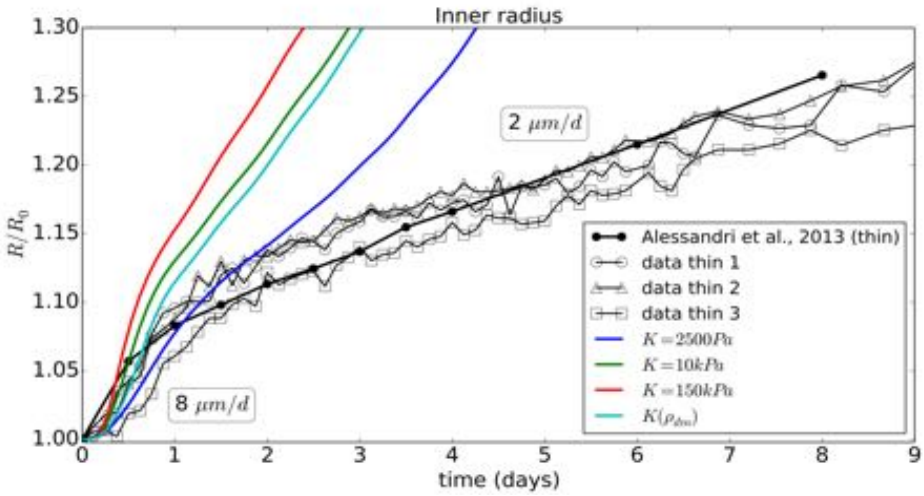

(a)

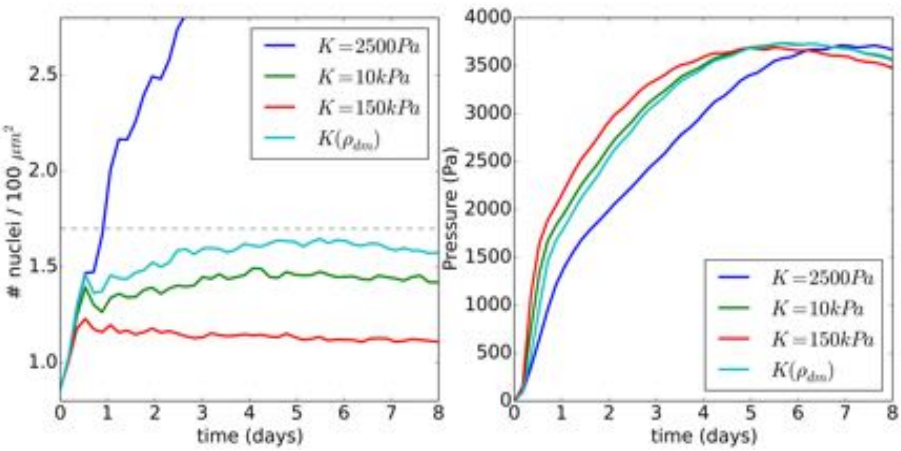

(b)

Figure 4: (a) Time evolution of the radius of the thin capsule, shown for the experimental data and the simulation using Model Ia, with parameter variation on the individual cell compressibility. Additional data points "data thin 1-3" were provided by P.N. (see *Supplementary material*) (b) Left: time evolution of the simulated curves for respectively cell density. The dashed horizontal line indicates the double cell density at $48h$. Right: pressure in the capsule versus time.

Strain hardening: Some authors reported strain hardening effects leading to an increased elastic modulus upon mechanical stress [36]. Stiffening of the cells could also occurs as the cytoskeleton gets denser [37]. To test the effect of strain hardening we replace the constant compression modulus with a linear increase of K with the "dry mass density" ρ_{dm}:

$$K(\rho_{dm}) = K_0 \rho_{dm} = K_0 \frac{V_{ref}}{V} \tag{2}$$

with $\rho_{dm} = V_{ref}/V \geq 1$. We choose $K_0 = 5000\,\mathrm{Pa}$ and $K(\rho_{dm} = 2) = 10\,\mathrm{kPa}$. In this scenario, K is initially smaller but gradually increase during compression, leading to a higher overall cell nuclei density

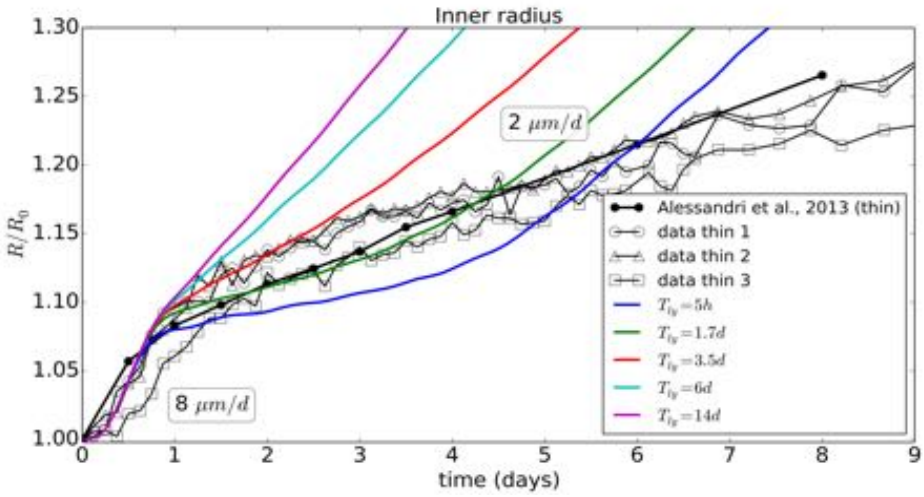

(a)

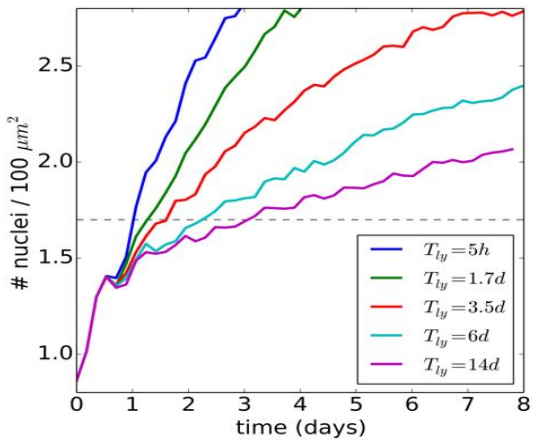

(b)

Figure 5: (top) (a) Time evolution of the radius of the thin capsule, shown for the experimental data and simulations using Model Ia, showing the effect of a parameter variation for the lysis time T_{lys}. (b) Time evolution of the simulated curves for respectively cell density.

(Fig. 4b). However, the stiffening does not solve the discrepancy between data and model simulation results. It allows a rapid nuclei density increase in a spheroid for low pressure but at the same time leads to higher mechanical resistance with increasing pressure. We adopt the stiffening in Model Ia.

In a next step we studied whether incorporating the effect of intrinsic volume loss of apoptotic cells due to lysis would lower the radius expansion and establish agreement between model and data. Lysis induces an irreversible water loss and decreasing of the volume of the cells (see *Methods* section 4.1.3). Contrary to *in vivo* experiments, there are no macrophages present to phagocytose the remaining cell bodies, and phagocytation by neighbor cells is very slow [21]. We studied lysis times $T_{lys} \in [5h, 14d]$ using Model Ia. For shorter T_{lys} the residual growth curves get closer to the experimental curves but largely fails to reproduce the the observed linear behavior (see Fig. 5). This is because lysing results in more compression and thus gradually stiffer cells. The effect becomes clear at very low lysis times ($T_{lys} = 5h$). Here, the initial behavior of the spheroid is determined by cells quickly loosing their volume (hence low resistance). Further in time,

a large stiff core forms which will eventually overcome the mechanical resistance of the thin capsule (see explanation above). Nevertheless, a $T_{lys} = 6d$ yields a good agreement with the cell nuclei density at $48h$ (Fig. 5b), and this is also relatively close to the apoptosis time found by fitting phenomenological growth laws for spheroids ($\approx 5d$) [38, 8]. On the other hand, it is still not possible to simultaneously fit growth and density curves with Model Ia.

In conclusion, no agreement between Model Ia and data could be found for a constant growth rate, neither by variation of the compression modulus, the magnitude of the lysis time, or by taking into account strain hardening.

2.4. Simulation of experiment I for thin capsules: compression inhibited growth rate

"Model Ib": In the following step we assume that the growth rate α depends on the degree of compressive stress according to Eq. 1. In "Model Ib", cells can enter G0 if the relative growth rate α/α_0 falls below a threshold α_{qui} between division and restriction point, here assumed to be after 1/4 of the cell cycle (H.III, Fig. 3).

With Model Ib we found a very good agreement between experimental data and simulation results for $\epsilon_{V_{tr}} \approx 0.35$, $n = 1, 2$ and $\alpha_{qui} \leq 0.33$ (Fig. 6a, Fig. 6b)). Low values of n do not discriminate, yet $n \geq 4$ results in a faster growth in the beginning but an experimentally not observed flattening of the residual growth ($n \to \infty$ leads to a plateau). Increasing α_{qui} to 0.5 results in a significant growth stall (see Fig. 6a). Increasing $\epsilon_{V_{tr}}$ results in a faster capsule dilatation over the whole period. We selected $\epsilon_{V_{tr}} \approx 0.35$ as optimal fit. The effect of $\epsilon_{V_{tr}}$ is shown in the thick capsule experiment (see next section, Fig. 7a).

Importantly, note that we still have a very good agreement when applying Model Ib to the free growing spheroids experiment simulation, see black full line in Fig. 2a. This shows that of the proposed growth function is still valid when compression effects are much lower.

So far we assumed cells to divide after their volume has doubled. Consequently, for a compression dependent growth rate, a cell subject to compressive stress has a longer cell cycle duration than an isolated cell. We also tested the assumption that a cell always divides after a fixed cell cycle time. In this case we find that the nuclei density is too large, as cells under compression tend to divide before their volume has doubled (Fig. 6b).

Finally, we also captured different growth dynamics of individual cells within their cycle. With Model Ib, we tested the hypotheses whether cells either have a growth rate, constant during the cycle (Eq. 16 in *Methods*) or rather an exponential increase (Eq. 17). Yet, the results are quite robust for these assumptions as we did not find any significant differences for the spheroid growth.

Concluding, with simulations using Model Ib a much better agreement with data could be obtained in case the cell divides after doubling its volume (even if this prolongs the cell cycle). A movie (Video 2) of this simulation is provided in the *Supplementary material*.

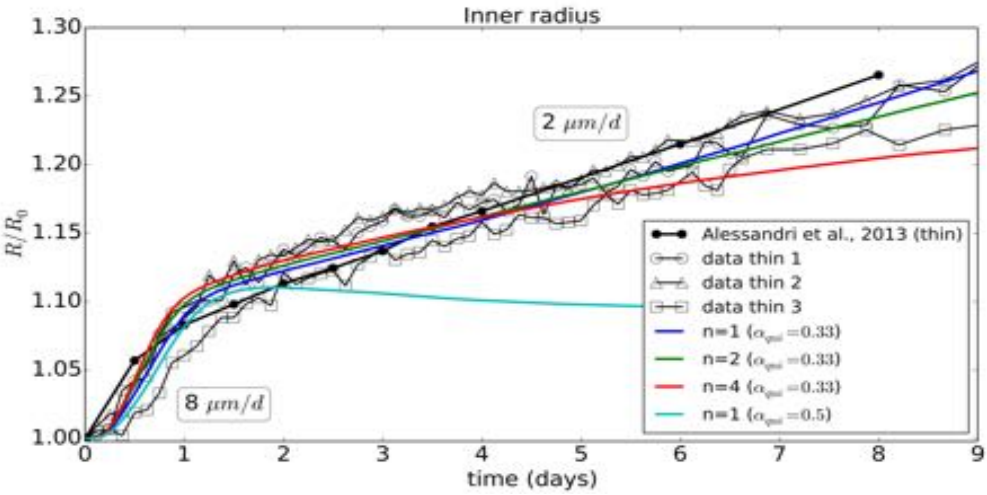

(a)

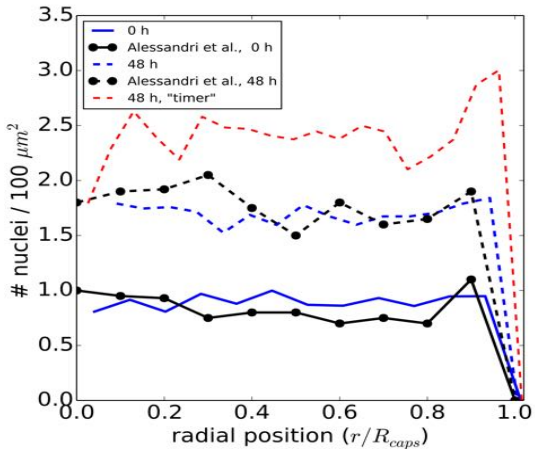

(b)

Figure 6: (a) Time evolution of the radius of the thin capsule for the experimental data and the simulations using Model Ib showing the effect of a parameter variation for n with $\alpha_{qui} = 0.33$, and $n = 1$ with $\alpha_{qui} = 0.5$. (b) Simulation and experimental values of the radial cell density in the spheroid at $T = 0h$, and $T = 48h$ for the optimal parameters. The model run with the same parameters, but in which cells divide after a fixed cycle time ("timer") is also shown.

2.5. Comparison of Model Ib for experiment I with thick capsule

For validation, we considered the thick capsule experiment ($H = 30\,\mu$m) running the simulations using Model Ib and found that the parameter set ($n = 1, \epsilon_{V_{tr}} = 0.35, \alpha_{qui} = 0.3$), close to the one for the thin capsule, gave the best fit.The results for the radial expansions are depicted in Fig. 7a, showing still a good agreement. For higher or lower values for the volumetric strain threshold $\epsilon_{V_{tr}}$, respectively, an overestimation or underestimation for the residual growth is observed.

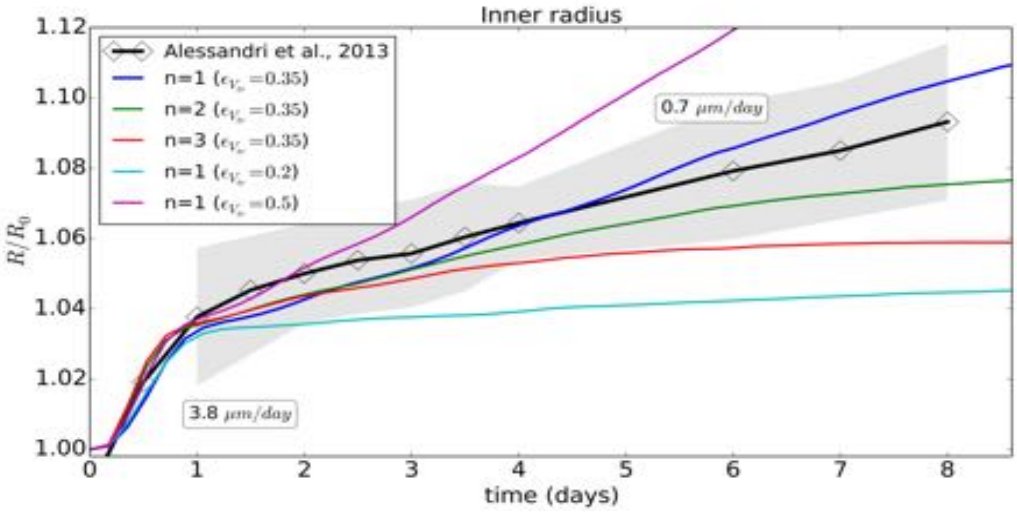

(a)

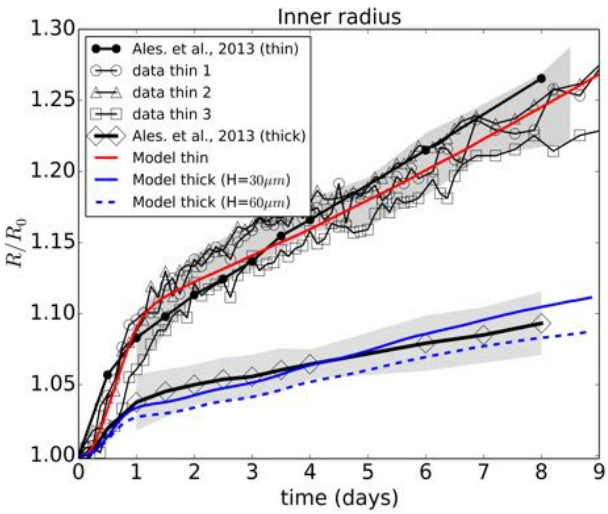

(b)

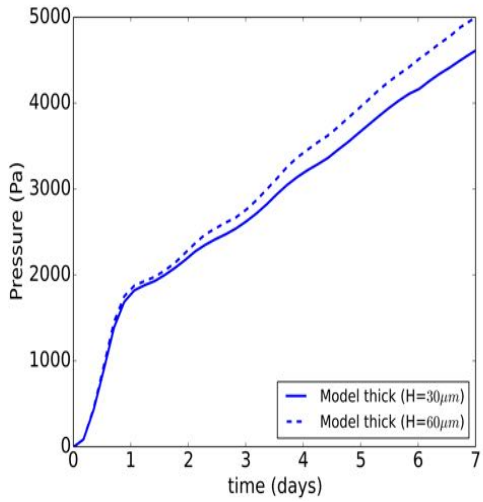

(c)

Figure 7: (top) (a) Time evolution of the thick capsule radius ($H = 30\,\mu$m), shown for the experimental data and the simulation with Model Ib, indicating the effect of the parameter n and $\epsilon_{V_{tr}}$. The errors on the thick capsule data are obtained from the spreading on the thin capsule data and indicated by the grey zone. (b) Global view of experiment I and II and respective model runs, including an additional run for a capsule wall thickness $H = 60\,\mu$m. (c) Simulated evolution of the average pressure in a capsule with $H = 30\,\mu$m and $H = 60\,\mu$m.

Values $n > 2$ resulted in a clear deviation the end of the observation period and were hence rejected. Because of a lack of additional data, the errors on the thick capsule data were estimated from the spreading on the thin capsule data, by determining the minimum - maximum intervals for the thin data. These are then rescaled by the ratio of thin - thick capsule dilatations and shifted on to the thick capsule curve.

To permit further validation of the model we also depict simulations for a capsule with thickness $H = 60\,\mu$m. This run predicts a slightly lower dilatation rate (Fig. 7b) yet the pressure increase per day in the capsule (Fig. 7c) is comparable with the $30\,\mu$m case, indicating a maximum for this cell line of about 2000 Pa/day.

2.6. Validation II: experiment II

Finally, we tested if the model calibrated with the experiments of the thin capsule for experiment I is able to predict the observed growth of CT26 multicellular spheroids in Dextran solution [8]. For this purpose the objective was to change our model developed for the capsule as little as possible. Dextran expels the water out of the spheroid and generates osmotic forces exerted to the outer cells, which then are transferred as compressive stresses to the bulk cells. The concentration of Dextran regulates the applied pressure. The growth rate at $p = 5\,$kPa is significantly lower than those in control spheroids. Strikingly, the freely growing spheroids in experiment II grow much slower than in Experiment I, revealing an overall linear but not exponential growth kinetics. This difference in behavior is likely to be a result of the culturing conditions.

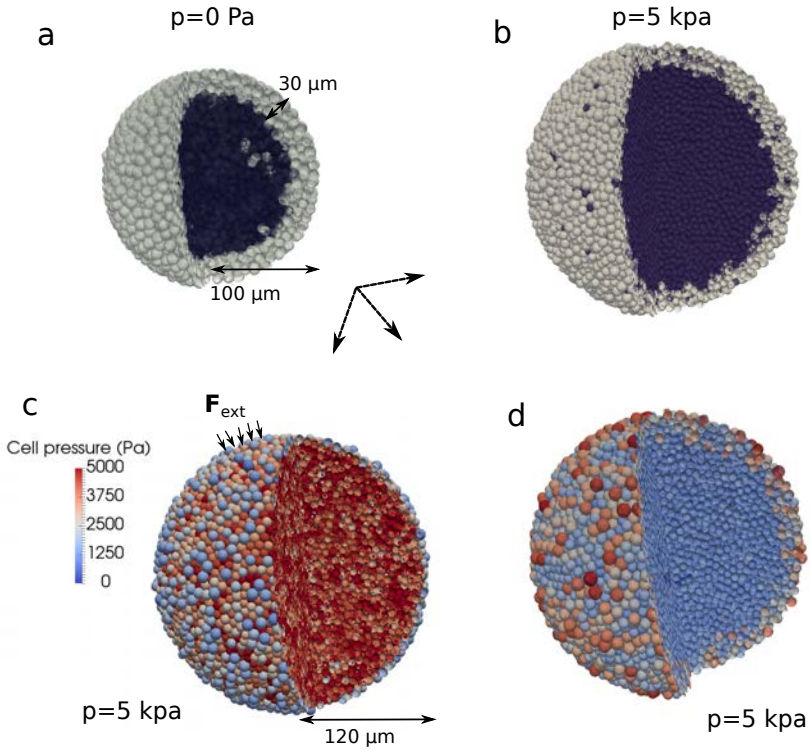

Figure 8: (a) Simulation snapshot at the beginning of a free growing CT26 spheroid ($R = 100\,\mu$m), indicating quiescent (dark) and proliferating cells (light). (b-d) Simulation snapshots of growing CT26 spheroids at $R = 120\,\mu$m during Dextran application ($p = 5\,$kPa), indicating quiescent and proliferating cells (b), individual cell pressure (c), and volume for the cells (d). Color coding: red is higher, blue is lower.

Model II: To take the different culture conditions that led to such a different outcome for free growth into account within our simulations, we in a first step simulated again the free growing spheroid. Linear

behavior is characteristic for a proliferative rim of constant size, with the size and spatial distribution of proliferating cells in the rim determining the speed of spheroid expansion ([39, 21]). To capture this effect without explicitly modeling the complex metabolism pertaining to the growth kinetics, for which much more data would be needed [21], we imposed a distinct layer of proliferating peripheral and quiescent bulk cells. As we do not simulate nutriments effects explicitly we assume all the cells in the bulk, from the beginning on, will go to rapidly a quiescent state but undergo no lysis as there is no increase in necrosis observed. The cells in the periphery remain proliferating. The discriminant for keeping a proliferating state is in the model translated to a threshold valued λ_{crit} which is measured from the edge of the spheroid onwards. Here, the edge of the spheroid is computed as the average of the radial positions of the most outer cells plus one mean cell radius (see Fig. 8a). We found that $\lambda_{crit} \sim 30\,\mu$m with cells adopting the same parameter set from the previous experiments ($n = 1, \epsilon_{V_{tr}} = 0.35, \alpha_{qui} = 0.3$), matches well with the free growing data (Fig. 9). This is referred as Model II. We then keep these values for the growth simulations in the presence of Dextran. In other work by Delarue et al. (2014) [33] slight cell elongations were reported towards the tumor center, which we neglected here to test whether the experimentally observed response of a growing tumor subject to osmotic stress can already be captured with the model originally developed for the capsule, with the only difference being an adaptation for the free growth conditions.

In the next step we incorporate the effect of Dextran in our so-calibrated model to study how compressive stress would impact the growth kinetics. In accordance with the known pressure-exerting effect of Dextran, we apply an external force only to the outer cells, directed towards the center of the spheroid, mimicking the osmotic effects which induce depletion-induced adhesion and an increase of the contact area between the cells [40]. The magnitude of the applied force on an outer cell i reads:

$$F_{ext,i} = F_0 \frac{V_i}{V_{i,ref}}, \tag{3}$$

where F_0 is calibrated such that the experimentally observed average cell pressure $< p_i >= 5\,$kPa is maintained inside the bulk of the spheroid during growth. As there is no confining volume, we use the *local* calibration approach to compute the contact forces, see *Methods* section 4.3). Within our model we find the pressure distribution in the bulk cells is quite homogeneous while for the most outer cells the pressure is locally lower because some of these cells are experiencing less contact forces from their neighbors (see Fig. 8c).

Remarkably, the slope of the growth curve obtained from a simulation with the model without any further adjustment matches very well with the data (see Fig. 9). This indicates that the response of the CT26 cells on compressive stress is robust and reproducible even if the cells are subject to different environmental conditions. Moreover, the surprisingly good agreement between model prediction and experimental observation suggests that the slight cell elongations observed in [33] might not be a fundamental determinant in the overall response of a growing tumor to external mechanical stress by osmosis. Perhaps the major contribution to the stress response is controlled by the proliferating cells that are mainly located close to the border. For additional test purposes we verified that, in agreement with the capsule runs, setting the growth parameters $\alpha_{qui} > 0.3$, $\epsilon_{V_{tr}} < 0.2$ or $n > 2$ resulted in a significant underestimation of grow (too many cells go into quiescence). To permit further validation, a run for a higher Dextran concentrations resulting in $< p_i >= 10\,$kPa is also given, indicating a significant decrease in growth.

Moreover, as proliferating cells, which are on average larger than resting cells, are preferentially localized at the border, the nuclei-nuclei distance is larger close to the border of the spheroid than inside (see Fig. 8d). This was also observed by Delarue et al. (2014) [8] and in freely growing spheroids [39].

3. Discussion

By establishing a quantitative model of growing multicellular spheroids subject to compressive stress calibrated with data on growth in an elastic capsule we were able to demonstrate that the stress response of a growing tumor is quantitatively robust and reproducible even if the cells grow under different conditions and the pressure is exerted by different methods. Given the enormous complexity of intracellular processes

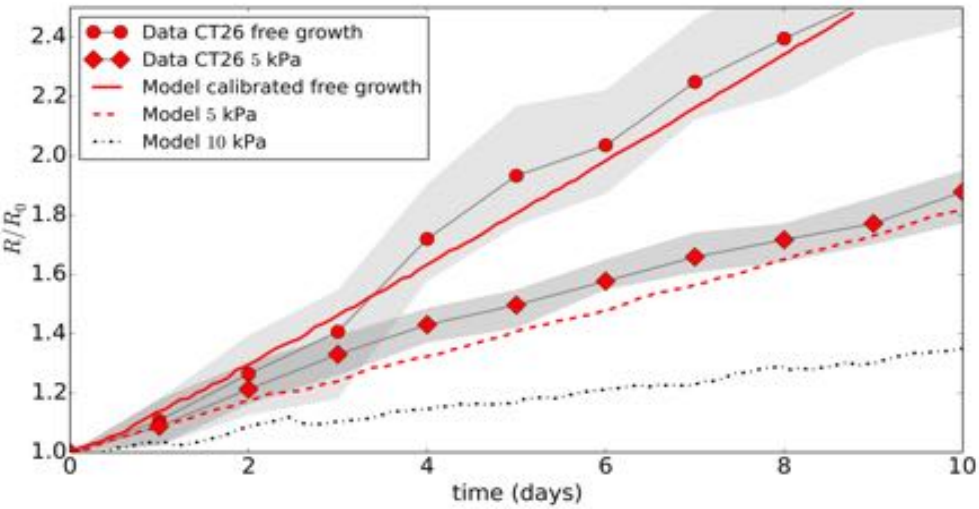

Figure 9: Time evolution of radius of the CT26 spheroid relative to its initial state. Data from [8] shown for free growth and at $p = 5\,\text{kPa}$. Runs with "Model II" are for free growth and $p = 5\,\text{kPa}$, and one additional run for $p = 10\,\text{kPa}$ as prediction. The grey zones indicate the min-max values of the data.

that participate in multicellular growth this is fascinating as it might open the possibility that largely separated functional modules may be identified and studied in separation without the need to analyze all interactions of the components of this module with the components of other modules. In particular, we first developed a model to study CT26 cells grown in an elastic thin and thick capsule, and then modified this model in a minimal way by taking into account the remarkably different growth behavior of freely growing tumor spheroids (i.e. not subject to compressive stress) to simulate the tumor growth response in a Dextran solution. The large difference in the growth curves for free spheroids not subject to any compressive stress indicated significant differences, however, the mechanical stress response was quantitatively the same. Without the model, it would have been very difficult to identify this equivalence. The key results of our analysis are: (R.I) with increasing compression the cell growth rate decreases. This relation could be well captured by a Hill function for the growth rate α that depends on the volumetric strain (Eq. 1), and a transition into quiescence if the growth rate felt below a threshold value. A sharp volume or pressure threshold below which no cell cycle entrance would occur anymore, is not compatible to the data. (R.II) Cells are compressible on long time scales, with a K increasing with the volumetric strain. (R.III) In the model, we have assumed that cells that have become necrotic are lysing, thereby losing up to a maximum of 70% of their initial mass. The death cells in the capsule embedded spheroids have a characteristic lysing time of $6d$. (R.IV) Cells divide when their dry mass has doubled during the cycle. A "timer" as a decision mechanism for dividing could not explain the data.

A particular point of concern all studies of spheroids is the appearance of cell death. Our work is based on the observations of Alessandri et al. (2013), who observed necrosis (CT26 cells, using FM4-64) in capsule confined cells, while their free growing spheroids exhibited the normal exponential growth for $R < 150\,\mu\text{m}$. In their experiments, Helmlinger et al. (1996) [4] observed a decrease in apoptotic (LS174T cells, using TUNEL) events during compression, while they also observed little necrosis (not measured) for spheroids with $R < 150\,\mu\text{m}$. They concluded that the haltered growth of the spheroids is mainly due to the increasing compressed state, which can be partially confirmed by our simulations (see Fig. 4). In the work of Delarue et al. (2014) [8], no increase of apoptosis (HT29 cells, using cleaved-caspase 3) was observed after 3 days for spheroids with $R \sim 100\,\mu\text{m}$. On the other hand, Cheng et al. (2009) [5] did observe an increase of necrosis (67NR cells, using propidium iodide) even in very small spheroids $R \sim 50\,\mu\text{m}$, yet mainly for the bulk cells. At the periphery, cells were still dividing. The fact whether necrosis occurs or not may well be dependent

on the cell type, but overall it seems that the peripheral cells are much less affected.

Clearly, the exact values of the parameters still need to be taken with caution and are expected to be cell-type-dependent. More experiments with different pressure conditions can validate the proposed growth law. Our modeling strategy bases on an *in silico* experiment, i.e., an abstracted experiment on the computer, where each individual cell was represented as modeling unit that could be equipped with those properties, actions and interactions that were considered as necessary to quantitatively explain the cellular growth response on mechanical compression. The implementation of cell-cell and cell-environment interaction directly accounts for physical laws with (in principle) measurable physical parameters which permit straightforward limitation of parameter ranges to those physiologically relevant. A particular challenge was to construct an individual agent based model that permits stable and robust simulations up to several tens of thousands cells under high compression. Under high compression cell displacements may have to be minimal, which rules out models operating on lattices unless the lattice size would be chosen a very small fraction of the cell diameter (in which case their loose their computational advantage). Thus, the requirements of constraining the parameters, and providing realistic simulation trajectories in time favored models operating in lattice-free space and following a dynamics simulated by equations of motion (as opposed to a Monte Carlo dynamics, that under some condition mimics a master equation). The prototype of lattice free models are center-based models that calculate the forces between cells as forces between cell centers. However, as explained elsewhere [18] this model type has significant problems in dealing with cell populations under large compressive stress i.e., with exactly the situation we are faced with in this paper. To solve this issue, we developed a deformable cell model which represents each individual cell in much greater detail as in center-based models but at the expense of much longer simulation times. As simulations with that model up to several thousands of cells were not feasible, we performed simulations with this model of characteristic multicellular configurations under large compressive stress and used the results to establish a new interaction force model within center-based models.

Finally, we mention that despite their limit on cell numbers, simulations with DCM can give valuable information on micro mechanics. In our study, we found that stiffer cells in a scaled capsule model more likely could cause a gradient in cell pressure from the border to the center of the spheroid than soft cells (see *Supplementary Material*). These potential effects are hard investigate to with center base models and prove the necessity of further development of high resolution models.

4. Methods

4.1. Center based model (CBM)

In CBMs cells are approximated as simple geometrical objects capable of active migration, growth and division, and interaction with other cells or a medium [41]. In CBMs the precise cell shape is not explicitly modelled but only captured in a statistical sense.

4.1.1. Equation of motion for the cells

The center of mass position of each cell i is obtained integrating a Langevin equation of motion, which summarizes all forces on that cell including a force term mimicking its micro-motility:

$$\Gamma_{ECM}\vec{v_i} + \Gamma_{c,cap}\vec{v_i} + \sum_j \Gamma_{c,c}(\vec{v_i} - \vec{v_j}) = \sum_j \vec{F}_{cc,ij} + \vec{F}_{mig,i} + \vec{F}_{cap,i} + \vec{F}_{ext,i} \tag{4}$$

We assume that the system is inertia less (very low Reynolds number) due to the high friction of the cells with their environment [42]. On the left hand side of this equation are the friction tensors for cell-ECM friction (Γ_{ECM}) cell-cell friction ($\Gamma_{c,c}$), and cell-capsule friction ($\Gamma_{c,cap}$), together with the cell velocities $\vec{v_i}$. If friction coefficients parallel and normal to the movement direction are different, the general form for the friction tensors can be explicitly written as

$$\Gamma_{ij} = \gamma_{\perp}(\vec{u}_{ij} \otimes \vec{u}_{ij}) + \gamma_{||}(I - \vec{u}_{ij} \otimes \vec{u}_{ij}), \tag{5}$$

with $\vec{u}_{ij} = (\vec{r}_j - \vec{r}_i)/||\vec{r}_j - \vec{r}_i||$, where $\vec{r}_i$, $\vec{r}_j$ denote the position of the centers of cell i and object j (I is the 3×3 identity matrix, $\otimes$ denotes the dyadic product) [18]. The individual cell friction coefficients are $\gamma_{\perp}$ and $\gamma_{||}$, respectively perpendicular and parallel to the movement direction. As experiments do not indicate ECM inhomogeneity or anisotropy, the cell-ECM friction matrix is considered to be diagonal.

On the right hand side of the equation of motion are the cell-cell repulsive and adhesive forces $\vec{F}_{cc}$, A force term $\vec{F}_{mig}$ mimicking the cell micro-motility, external forces $\vec{F}_{ext,i}$ (e.g. due to Dextran), and the interaction force experienced by the cell from the capsule $\vec{F}_{cap}$. The latter is purely repulsive as cells cannot adhere to the capsule. The micro-motility force of cell i is mimicked by a Brownian motion term with zero mean value and are uncorrelated in time:

$$< \vec{F}_{mig,i} >= 0 \tag{6}$$

and

$$< \vec{F}(t_1)_{mig,i} \otimes \vec{F}(t_2)_{mig,i} >= A\delta(t_1 - t_2). \tag{7}$$

The amplitude tensor A of the noise autocorrelation function is generally not known. One may draw a formal analogy to a colloidal particle moving in a homogeneous isotropic fluid [43]. In this case $A = 2D\gamma^2 I$, D being the cell diffusion constant, γ the friction coefficient of a cell in the medium and I the unity matrix. This result could be obtained if the cell moves in an isotropic, homogeneous environment for which $\gamma_{||} = \gamma_{\perp}$. However, keeping in mind a fluctuation-dissipation theorem for cells do not exist, and the random movement of cells is controlled largely by active migration processes such as anchoring and releasing filopodia but not by random collisions with fluid particles, the parameters in tensor A are largely controlled by the cell itself.

As the ECM material is not represented explicitly here, the above equations do not conserve total momentum due to the micro-motility term. Yet as the cells are growing in a spherical aggregate, and the central position of the capsule does not change, this poses no problem. The system of Eq. 4 needs to be integrated numerically until the simulation time surpasses the total duration of the experiment which is 8-10d. Eq. 4 results in a linear problem with a sparse symmetric matrix, which can be solved efficiently by a Conjugate Gradient method [44] and an explicit Euler integration scheme.

4.1.2. Adhesive and repulsive forces

Interphase cells are approximated by homogeneous, isotropic, elastic and adhesive spheres which split into two adherent cells during mitosis. For moderate deformations, the forces between pairs of spheres have been shown to resemble the Johnson-Kendall-Roberts (JKR) force model which takes into account the hysteresis behavior in different forces at the same distance for cells that approach each other and those which are pulled apart [14, 40]. In the simulations considered in this paper the cells are under permanent compression hence detachment does not occur. In that case, as illustrated in [45, 41], one can approximate the interaction force by the simpler extended Hertz model, that corresponds to adding an adhesion term to the Hertz force. The Hertz force model represents the limit of the JKR model in absence of adhesion. The extended Hertz model can be analytically solved while the JKR model would require numerical iterations hence would significantly slow down the simulations.

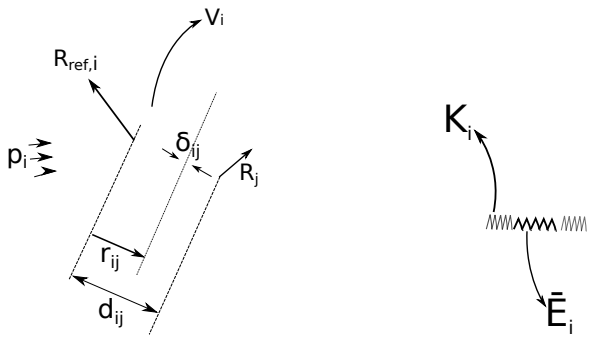

(a) (b)

Figure 10: Contact between two cells defining (a) the distance d_{ij}, virtual overlap δ_{ij}, reference radius $R_{ref,i}$, actual radius R_i and volume V_i, and (b) the internal stiffness (compressibility K_i) and contact stiffness $\tilde{E}_i$.

Consider first two non-adhesive cells i and j in contact and with their centers separated by a distance $d_{ij} = ||\vec{r}_j - \vec{r}_i||$. If d_{ij} becomes moderately smaller than the sum of their radii hence leading to moderate deformations of the cells, according to Hertz theory the contact force $F_{rep,ij}$ develops as a function of the virtual overlap $\delta_{ij} = R_j + R_i - d_{ij}$:

$$F_{rep,ij} = 4/3 E_{ij} \sqrt{R_{ij}} \delta_{ij}^{3/2} \tag{8}$$

in which E_{ij} and R_{ij} are defined as

$$E_{ij} = \left(\frac{1-\nu_i^2}{E_i} + \frac{1-\nu_j^2}{E_j} \right)^{-1} \text{ and } R_{ij} = \left(\frac{1}{R_i} + \frac{1}{R_j} \right)^{-1}$$

with E_i and E_j being the cell Young's moduli, ν_i and ν_j the Poisson numbers and R_i and R_j the radii of the cells i and j (see Fig. 10a), respectively. An important issue though, is that the Hertz model does not take cell forces due to volume reduction into account, so that even in simulations with incompressible cells ($\nu = 0.5$) unrealistic compression could still appear. To include volume compressibility in the center-based approach, we drop the assumption of E_i being a constant in our model, and we define an apparent Young modulus $\tilde{E}_i$ that increases as function of the cell density (see section 4.3).

The adhesive force term between cells can be estimated as proportional to the contact area and the energy of the adhesive contact W [45]:

$$F_{adh,ij} = -\pi W R_{ij}. \tag{9}$$

The total interaction force is then $\vec{F}_{cc} = \vec{F}_{rep} + \vec{F}_{adh}$, and acts along the line connecting the centers of two interacting spherical cells.

4.1.3. Individual cell volume

In tissues under high pressures, cell compressibility may become an important factor. In our model we consider both the compressibility of individual cells and that one of the whole spheroid. The bulk modulus K_i describes the resistance of a matter to uniform compression. It is the inverse of the compressibility κ_i describing how far a volume of matter is able to change upon compressive stress:

$$K_i = -V_i \frac{dp_i}{dV_i} = E_i/3(1-2\nu) = 1/\kappa_i. \tag{10}$$

The compressibility of the cells is mainly controlled by the elastic response of a cytoplasmic constituents. The observed volume change in general depends on the speed of compression. For slow compression, water can be squeezed out of cells (and tissues), while for fast compression, water would yield incompressible resistance. Integration of the above equation for K_i yields the cell volume V_i as a function of the pressure (compressive stress) on cell i, the compression modulus and the reference volume that the cell would have in isolation:

$$\log(\frac{V_i}{V_{ref,i}}) = -\frac{p_i}{K_i}. \tag{11}$$

Here $V_{ref} = 4/3\pi R^3_{ref,i}$ is the uncompressed cell volume ($R_{ref,i}$ (considered as constant for a quiescent cell), see Fig. 10).

We assume that as a consequence of internal friction and by remodeling of the cytoskeleton, a cell subject to compressive stress adapts its volume only with a certain delay. We capture this by following differential equation:

$$\gamma_{int}\dot{\epsilon}_{V,i} + K_i\epsilon_{V,i} = -p_i \tag{12}$$

where $\epsilon_V = -\log(V/V_{ref})$ is the volumetric strain and γ_{int} is a lumped parameter expressing the relaxation behavior after an imposed change of the cell volume. The equation is basically equivalent to a Kelvin-Voigt dynamical system. The logistic strain ϵ_V captures large strains. For small deviations $V \approx V_{ref}$ the known relation $\log(V/V_{ref}) \approx (V - V_{ref})/V_{ref}$ is recovered.

The friction parameter γ_{int} is related to the relaxation time by $T_{rel} = \gamma_{int}/K_i$ for a single cell (and by an analogous argument, for the whole spheroids). The relaxation period may range from several seconds or minutes up to hours, depending on how long the stress has been applied [46, 47, 8]. This phenomenon is likely to be due to both intracellular and intercellular reorganizations. In our simulations, we assume characteristic cell relaxation time $T_{rel} = \mathcal{O}(1h)$ for a viable cell [48].

4.1.4. Measures for stress

As summarized in ref. [18], several measures have been used to quantify the mechanical stress in multicellular configurations within CBM simulations. Here we apply a concept of virial stress that originates from stress definition in molecular dynamics [49, 50, 51], as it allows to calculate the full stress tensor. As the motion of cells as opposed to that of molecules is overdamped, the kinetic contribution can be dropped, and the stress of a cell i due to contact forces $\vec{F}_{ij}$ with other cells is calculated as:

$$\sigma_i = \frac{1}{\mathcal{V}_i}\sum_j \left(\vec{F}_{ij} \otimes \vec{r}_{ij}\right) \tag{13}$$

where $\vec{r}_{ij}$ is the vector pointing from the center of cell i to the cell j with $||\vec{r}_{ij}|| = (d_{ij} + R_i - R_j)/2$ (see Fig. 10), and $\mathcal{V}_i$ is the *sampling* volume. This measure was originally defined for small volumes containing an ensemble of molecules, however, we apply it here to approximate the stress tensor for individual cells, by taking actual volume of the cell as the sampling volume.

The external pressure p on a cell i is given by:

$$p_i = \frac{1}{3}tr(\sigma_i). \tag{14}$$

A justification for this formula is given in [18]. From each stress tensor, we can also derive the following quantity that accounts only for deformational stress:

$$S = \sqrt{0.5\left[(\sigma_{xx} - \sigma_{yy})^2 + (\sigma_{yy} - \sigma_{zz})^2 + (\sigma_{xx} - \sigma_{zz})^2\right] + 3\left[\sigma_{xy}^2 + \sigma_{yz}^2 + \sigma_{xz}^2\right]}. \tag{15}$$

In addition, we can also derive the principal stress directions $\{n_1, n_2, n_3\}$ and eigenvalues $\{\sigma_1, \sigma_2, \sigma_3\}$ by diagonalization of Eq. 13, yielding important information on how principal stresses on the cells are oriented. This is for example illustrated in Fig. 12a. We used Cardano's method for diagonalization of Eq. 13.

4.1.5. Cell growth, mitosis, and lysis

Our basic model assumes constant growth rate during the cell cycle and updates the volume $V_{ref,i}$ of cell i in time as

$$\frac{dV_{ref,i}(t)}{dt} = \alpha_{const,i}, \tag{16}$$

with $V_{0,i} = V_{ref,i}(0)$ the initial volume of the cell and α_i the growth rate. Alternatively, one could also assume that cell volume increases exponentially during the cell cycle:

$$\frac{dV_{ref,i}(t)}{dt} = V_{ref,i}(t)\alpha_{exp,i}, \tag{17}$$

with $\alpha_{exp,i} = \log(2)\alpha_{const,i}/V_{0,i}$. Several studies show that cell growth is not constant during the cell cycle [23, 24, 25, 26], yet no consensus or universal growth law could be inferred. In this work we have studied the two different assumptions for the growth rate. However, note that this work addresses the time scale of growth hence growth rate variations on time scales of less than an hour minutes turned out to be negligible.

We have studied two alternative implementations for cell division. As far as either the volume or the duration of the cell in the cell cycle have passed a threshold value, we replace the mother cell by two daughter cells which are placed very close to each other [45, 15]. This algorithm is different from the approach where cells deform into dumbbells in mitosis phase [41, 52]. In our model two daughter cells are created next to each other instantaneously. During the mitosis period (which takes about $1.5h$) the daughter cells do not grow. However, the two newly created cells can generate short artificial pressure peaks which dissipate during the division time course. To reduce these peaks, we have implemented an algorithm that (1) ensures the mother cell divides in the direction of the least stress as derived from the local stress tensor (see *Methods* section 4.1.4), and (2) a local energy minimum is sought by varying the distance between the daughter cells and computing the interactions with the other cells. While this algorithm reduces the pressure peaks, we did not see significant differences in the results with the case of using no precaution algorithm.

Cells dying either by apoptosis or necrosis eventually undergo lysis, whereby they gradually shrinks. The process is generally slower *in vitro* compared to *in vivo* where macrophages are around to digest the dead cells [21]. Cristini et al. [12] modeled lysis in ductal carcinoma explicitly as a volume decrease $V = V_0 \exp(-t/T_{lys})$ with a time constant T_{lys} of 1 to 5 days in their simulations. However, no pressure effects were considered in their simulations. In experiment I the necrotic core appeared very solid like, indicating that the water was drained as a consequence of the high pressure. We mimic the lysing process by setting first $V_{ref,i} \to \phi V_{ref,i}$ after necrosis, where ϕ is the volumetric solid mass fraction. In the model necrotic cells will not immediately acquire this new volume, but after a transient depending on the applied pressure and the internal frictional resistance γ_{int}. Note, as explained above, the cell volume change is governed by Eq. 12. The parameter γ_{int} is thus reset during lysis using the relation $\gamma_{int} \sim KT_{lys}$.

4.2. Deformable Cell Model

Deformable cell models are able to capture the complex shapes of cells and describe forces onto subcellular level [18, 53, 54, 55]. In a basic DCM the cell surface is discretized by a number of nodes which are connected by viscoelastic elements interacting via pairwise potential functions, creating a flexible scaffolding structure with arbitrary degrees of freedom per cell. The discretization can be extended to the entire cell volume and even organelles be represented. The nodes at the boundary form a triangulated structure, accounting for the mechanical response of the membrane and cortical cytoskeleton (see Fig. 11). The forces in DCM originate from both cell-cell interactions and intracellular interactions and are described by viscoelastic elements, bending resistance of the surface, and cell volumetric compressibility. We briefly describe the basic components.

The basic equation of motion in DCM is formally the same as for the center based model Eq. (4), but is now applied to each node i of the cell:

$$\sum_j \Gamma_{nn,ij}(\vec{v}_i - \vec{v}_j) + \Gamma_{ns,i}\vec{v}_i = \sum_j \vec{F}_{e,ij} + \sum_m \vec{F}_{m,i} + \vec{F}_{vol,i} + \sum_T \vec{F}_{T,i} + \vec{F}_{rep,i} + \vec{F}_{adh,i} \tag{18}$$

with Γ_{nn} and Γ_{ns} the matrices here representing node-node friction and node substrate friction. The latter one can be obtained by considering the CBM substrate friction coefficient divided by the number of nodes at the surface of the cell.

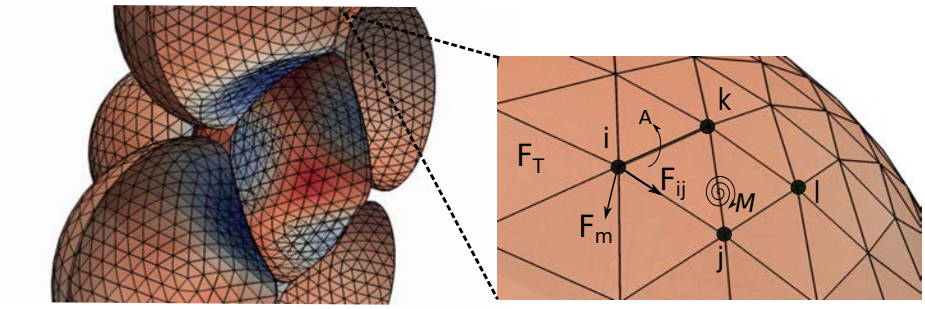

Figure 11: (left) DCM representation of several adjacent cells. (right) Detail of nodal structure building cell surface and depicting the forces that work on them.

The individual elements between the surface nodes are represented by classical linear spring-damper systems. The force between the nodes both capture the elastic response of the cortical cytoskeleton. When the elastic and dissipative components are added, one acquires the well known Kelvin-Voight element representing a solid like behavior. Let us now first consider the in-plane forces originating from the cortical cytoskeleton. The vector force between two nodes i and j read (see Fig. 11):

$$\vec{F}_{ij} = \vec{F}_{e,ij} + \vec{F}_{v,ij} = -k_s(\vec{d}_{ij} - \vec{d}_{0,ij}) - \gamma\vec{v}_{ij}, \tag{19}$$

where $\vec{F}_{e,ij}$ and $\vec{F}_{v,ij}$ are the elastic and dissipative forces, k_s is the spring constant, γ represents the dissipation, $\vec{d}_{0,ij}, \vec{d}_{ij}$ are the initial and actual distance vectors, and $\vec{v}_{ij}$ is the relative velocity between the nodes, respectively.

The surface bending resistance is incorporated by the rotational resistance of the hinges determined by two adjacent triangles $\alpha = \{ijk\}$ and $\beta = \{ijl\}$. This defines a moment M:

$$M = k_b sin(\theta - \theta_0) \tag{20}$$

where k_b is the bending constant, and θ is determined by the normals to the triangles $\vec{n}_\alpha, \vec{n}_\beta$, with θ_0 being the angle of spontaneous curvature. The moment M can be transformed to an equivalent force system $\vec{F}_m$ acting on each of the nodes of the triangles. We note hereby that $\vec{F}_{m,i} + \vec{F}_{m,j} + \vec{F}_{m,k} + \vec{F}_{m,l} = 0$.

Importantly, the parameters of the spring network can be related to macroscopic elastic constants. The linear spring constant k_s (for a sixfold symmetric triangulated lattice) can be computed from the Young modulus E_{cor} of the cortex with thickness h_{cor} by [37, 56]

$$k_s \approx \frac{2}{\sqrt{3}} E_{cor} h_{cor} \tag{21}$$

The bending stiffness of a (thin) cortex is in the same way approximated by

$$k_b \approx \frac{E_{cor} h^3}{12(1-\nu^2)} \tag{22}$$

where ν is the Poisson ratio ($= 0.3$ for an equilateral 2D network of linear springs). For a more a more in depth analysis relating the spring force parameters to macroscopic constants, we refer to literature [57, 56, 58].

To avoid large deformations of the triangles in the network, an extra force F_T, proportional to the area expansion of the individual triangles is added:

$$F_T = k_A(A - A_0)/A_0 \tag{23}$$

Here, A_0 and A are the initial and the current areas of the triangle, and k_A is the area compression stiffness. The forces $\vec{F}_{T,i}$ are summed over all triangles of the cell and transferred to the nodes in the direction perpendicular to the opposite vertex edge of that node. We chose k_A such that the influence on the membrane elasticity is minimal, yet triangle deformations are minimized.

The volume penalty forces $\vec{F}_{vol,i}$, reflecting the bulk compressibility of the cytoplasm, are computed from the internal pressure using the volume change and compressibility modulus of the cytoplasm K. In our simulations we can safely assume K reflects the overall cell compressibility including the cortex, as in its physiological range of elasticity, the cortex contributes little to the overall bulk modulus of the cell, i.e. $K \gg E_{cor} h_{cor}/R_{cell}$ ([35], own test runs). The pressure applied to the cell is therefore approximately given by:

$$p = -K \log(\frac{V}{V_0}) \tag{24}$$

The volume V of the cell is computed summing up the volumes of the individual tetrahedra that build up the cell. The forces $\vec{F}_{vol}$ on the nodes are perpendicular to the cell surface and can be obtained by multiplying the pressure with the surface area assigned to each node. In principle, internal nodes and elements could be added to model the elastic response of the internal cytoskeleton explicitly which would introduce shear stress components, but we do not incorporate this option here as we assume the multi cellular system is compression dominated.

Interactions between neighboring cells are accounted for by introducing repulsive $\vec{F}_{rep,i}$ and adhesive forces $\vec{F}_{adh,i}$ between nodes belonging to different cells. The sum $\sum_i \vec{F}_{rep,i}$ reflects excluded volume forces and determines the total contact force on the cell. Unlike in CBM, the cell bodies in contact do not overlap and therefore triangles belonging to different cells will be repelled when approaching too close to each other. These forces are modeled using the contact model as described in [59]. For consistency with the CBM we chose the model components of the DCM such that cells are inherently isotropic. However, in principle anisotropy could be included by representation of the cytoskeleton. For the model parameters in the DCM, see Table 1.

4.3. Calibration of the contact forces using a Deformable Cell Model

During the process of compression, cells will rearrange and deform to a closer packing. As discussed above, common models to model the interactions between cells (such as Hertz, JKR, extended Hertz, Lennard-Jones, etc.) base on pair-wise interaction force calculations and do not take into account the effect of volume compression emerging from the simultaneous interaction of many cells [18, 41]. In simulations using these interaction force models, the apparent volume (as seen in the simulation) that the spheroid occupies upon strong compression may become much smaller than consistent with the material parameters;

even incompressible cells having Poisson ratio $\nu = 0.5$ reduce their volume [18, 60]. The deformable cell model (DCM) does not have this shortcoming, but can only handle a limited amount of cells in reasonable computing time on standard desktop computers, which is why it was not amenable to simulate the whole spheroid growth in the capsule. In this work we propose an solution that largely overcomes the artifact of CBMs by correcting the interaction force in the CBM based upon numerical compression experiments performed with the DCM (Fig. 12). Note, that in these compression simulations with the deformable cell model mimicking isotropic cells, cell shaped are distorted near the capsule border. This is in line with the shapes one would infer from the position of the cell nuclei in the capsule experiments [9]. In the CBM, shape is not explicitly displayed but as we calibrate the forces and pressure of the CBM with the DCM, these mechanical effects in growing tumor spheroids should be captured.

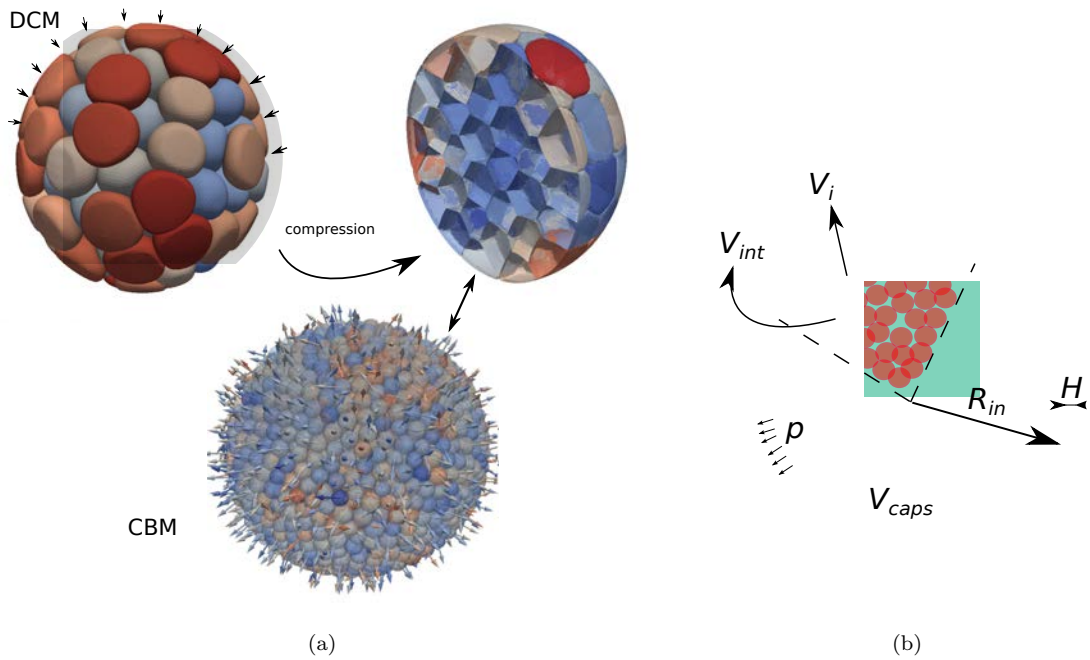

Figure 12: (a,top) Cartoon illustrating the compression experiment using deformable cells in a capsule to calibrate the center based model. (a, bottom) Equivalent compression experiment using the center based model with indication of the maximal principal stress directions of the cells in the capsule during compression using the virial formula. (b) Cartoon showing the volume compartments V_i, V_{int} and V_{caps} in a capsule with thickness H.

In order to obtain an estimate for the repulsive contact forces in CBM in case of many cell contacts, we have constructed a multicellular DCM experiment with ~ 400 cells initially positioned in a closest sphere packing. The outer cells are then pushed quasi-statically (to avoid friction effects) towards the central cells using a shrinking large hollow sphere encompassing the cells (see Fig.12a, we assume that this capsule wall is rigid). The cells have the same size (yet, taking into account a moderate variable cells size does not affect the results). However, in the DCM those cells close to the capsule border are apparently deformed as it is observed in [9]. At the point of confluence (outer cells touching the capsule wall), the DCM cells exert a total interaction force $F_{cap} = \sum_i F_{cap,i}$ on the capsule wall. This force is converted to a global pressure $p_{cap} = F_{cap}/A_{cap}$ where A_{cap} is the inner surface area of the capsule. We then obtain the curve of the pressure p_{cap} as a function of the volume fraction, defined as $\epsilon_{int} = V_{int}/V_{cap}$ where $V_{int} = V_{cap} - \sum_i V_{cell,i}$ is the volume of the space in between the cells and V_{caps} is the total capsule volume (see Fig. 13, solid green line).

From literature we adopted $E_{cor} \approx 2400\,\mathrm{Pa}$, $h_{cor} \approx 100\,\mathrm{nm}$ and $\nu_{cor} \approx 0.5$ [35]. This results in a cortical

stiffness $E_{cor}h_{cor} = 0.24\,\mathrm{mN/m}$, close to values deduced from other experiments performed on fibroblasts [61]. The compressibility of the cytoplasm was set to $K = 5000\,\mathrm{Pa}$. To study the effect of cell cortex stiffness, needed below to understand the pressure-volume relationship under moderate and strong compression, we have also performed a DCM simulation with a 10 times higher E_{cor} (Fig. 13, blue curve), showing a quicker response with respect to the compression. For a higher interstitial volume fraction ($\epsilon_{int} \approx 0.06$), the compressibility of the spheroid is about 1000 Pa, but at high compression ($p_{cap} \geq 1000\,\mathrm{Pa}$, i.e. $\epsilon_{int} \leq 0.01$) both curves appropriately converge largely. Thus, for high interstitial volume fractions the compressibility of the DCM spheroid is mainly influenced by elastic modulus of the cortex while for low fractions the main contribution is the compressibility of the whole cell.

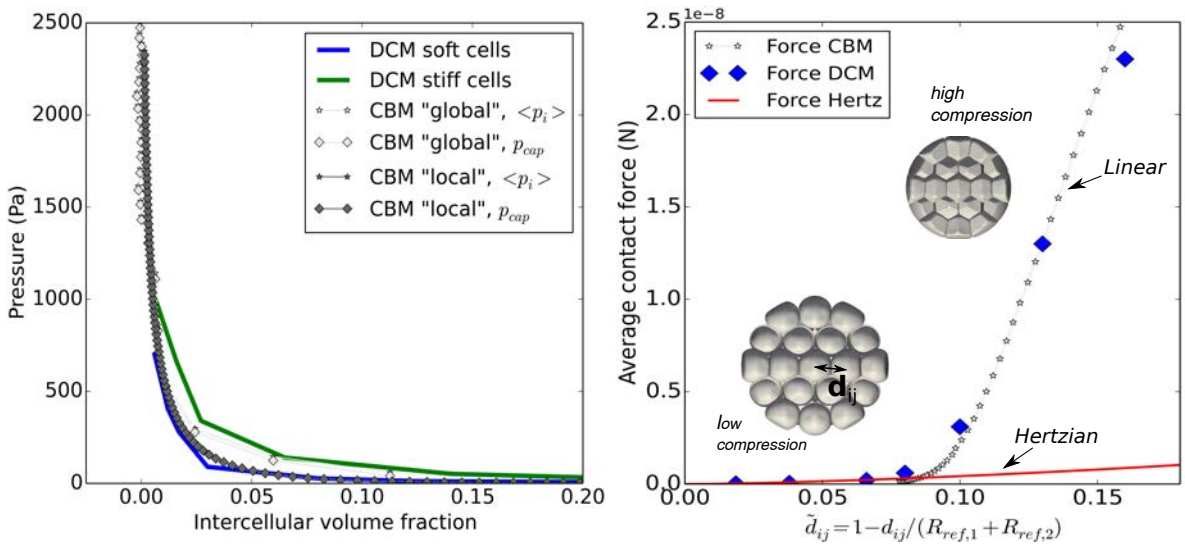

Figure 13: (left) Pressure curves during compression of the spheroid as a function of the intercellular volume fraction simulated with the DCM and the corrected CBM. The green solid line is the compression curve for DCM cells with physical parameters values as mentioned in the text, the blue line is from a comparable simulation for cells that have a 10 times stiffer cortex. The pressure for CBM was computed using both the capsule pressure and average virial stress per cell based on a *local* and *global* calibration approach. (right) Average $\tilde{d}_{ij}$ versus average contact force for the DCM and CBM simulation. Both curves exhibit an initial Hertz regime, followed by a volumetric compression (linear regime). The uncorrected Hertz force is indicated by the red line. A representative movie (Video 3) of these simulations is provided in the *Supplementary material*)

There are a few ways of calibrating the CBM contact forces. One possibility could be using Voronoi tessellation, providing a realistic estimate of the volumes and the contact areas of the individual cells in close packing [15] which would in turn give us the pressure and forces acting on the cell. However, this method is expensive in 3D and can be cause difficulties in handling the boundary cells.

Local approach, free spheroid

We try to estimate the degree of packing around one cell by using the the distances between that cell and its neighbors. During the DCM compression experiment we measure all the contact forces between a bulk cell i and the surrounding cells, which gives us the pressure and volume change on that cell, as a function of their relative positions, $\tilde{d}_{ij} = 1 - d_{ij}/(R_{ref,i} + R_{ref,j})$. The distance d_{ij} is computed as the length of the vector connecting the two center of masses of the cells, with $R_{ref,i}$ computed as $(\frac{3}{4\pi}V_{ref,i})^{1/3}$. The average contact force of the central cell with its neighbors as a function of the cell to cell average distance $\tilde{d}_i = \sum_{j=1}^{N_c} \tilde{d}_{ij}/N_c$ (N_c = number of contacts) is depicted in Fig. 13b, blue . We find that this contact force curve still can

be characterized as initial Hertzian contact for $\tilde{d}_i < 0.08$, but is after a transition zone followed by a linear behavior ($\tilde{d}_i > 0.1$). The first part in this curve is largely determined by the mechanical properties of the cortex and the changing contact area of the cells, whereas the behavior at larger compression is determined by the bulk modulus of the cells.

We have developed a CBM calibration approach where we keep the original Hertz contact law but modify the apparent modulus $E_i \rightarrow \tilde{E}_i$ of the cell as the intercellular spaces become smaller. In other words, the apparent Young's modulus gradually increases in Eq. 8 as the cells get more packed, based on the simple reasoning that indenting a piece of material with another object gets more difficult when confined. Thus, total strain of the cell is composed of a deformation of the cortex largely determined by the apparent Young's modulus $\tilde{E}_i$, and the volumetric compression, determined by K_i. Conceptually, the mechanics is equivalent to putting two springs with different stiffnesses in series, see Fig. 10b. The volume (and radii) of the cells are adapted using Eq. 12. It is important to stress here that $\tilde{E}_i$ only affects the apparent cortex stiffness of the cell through Eq. 8, while the bulk modulus (Eq. 10) is determined by the original cell Young's modulus E_i.

The challenge now lies in determining $\tilde{E}_i$ as a function of the compactness of the spheroid. We have achieved this by introducing a function that depends on the *local* average distance $\tilde{d}_{ij}$ for each cell:

$$\tilde{E}_i(\tilde{d}_i) = \begin{cases} E_i & 0 \leq \tilde{d}_i \leq 0.08 \\ a_0 + a_1\tilde{d}_i + a_1\tilde{d}_i^2 + a_3\tilde{d}_i^3 + a_4\tilde{d}_i^4 & 0.08 < \tilde{d}_i \end{cases} \tag{25}$$

in where a_0, a_1, a_2, a_3 and a_4 are fitting constants (see appendix B). They are calibrated so the function is monotonically increasing and results in an optimal fit for the pressure - volume fraction (see Fig. 13, left). The corresponding average contact cell-cell force $F_{cc,i}$ for the spheroid are plotted next to the average DCM contact force. These curves do not match exactly, but follow each other closely (Fig. 13, right).

Global approach, confined spheroid

If compression rates are sufficiently slow as is the case in the capsule experiment, cells in the spheroid may find the time to reorganize and "distribute" the stress isotropically and homogeneously over the cells in the spheroid. In this presumption, we computed the packing assuming that the intercellular spaces in the capsule are homogeneous over the spheroid during compression (see Fig. 12b). This allows us to introduce the *global* intercellular volume fraction ϵ_{int} and the cellular fraction ϵ_{cells} for which we have :

$$\epsilon_{int} + \epsilon_{cells} = 1, \tag{26}$$

with $\epsilon_{cells} = V_{cells}/V_{caps}$. We can now use ϵ_{cells} to re-parameterize Eq. 25. The apparent Young's modulus $\tilde{E}_i$ increases for all cells equally with ϵ_{cells} being the equivalent of $1 - \tilde{d}_{ij}$ in the previous approach.

Both CBM simulations with different calibration approaches then results in a curve that also closely follows the DCM curve. Compared to the local approach the curve for the global approach is smoother and less sensitive to the friction parameters and the radius distribution of the cells as it represents an average over all cells disregarding local fluctuations. For high pressures ($p > 2\,\text{kPa}$, both curves become nearly parallel. On the other hand, the local approach does not require the enclosed (capsule) volume and hence can be used as a general interaction force of individual cells upon volumetric compression. However, we have verified that the mutual differences for all simulations involving growth in the capsule are no more than 7% (see *Supplementary material*).

Importantly, the pressure curves for the CBM in Fig. 13 only show little mutual difference when using the average virial pressure for all cells, $< p_i >$, and the capsule pressure p_{cap}. In addition, it might be also interesting to look at the principal stresses (indicated in Fig. 12a by arrows) computed by Eq. 13. One clearly observes that the direction of maximal stress is pointed radially for the border cells, while minimal stress direction in pointed tangential to the capsule wall. This is equivalent to the DCM simulations where the cells have a flattened shape of at the border of the capsule (see Fig. 15, *Supplementary material*). Finally, we must emphasize that there is no explicit representation of ECM in the model. We assume the ECM fraction is rather small and approximately homogeneously and isotropically distributed in the intercellular spaces. Our model should be regarded as a cellular spheroid immersed in a fluid-like environment with a permeation time typically shorter than the duration of the experiment.

4.4. Elastic Capsule Model

The capsule is made of an quasi-incompressible alginate gel exhibiting a strain hardening behavior. The stress-strains relationship was measured in a stretching experiment of an thin alginate cylinder. Strain hardening behavior was observed for strains $> 15\%$. In case of a thick walled capsule, the expansion strain is low and hence linear elasticity can be applied. We refer to the hollow sphere example as described in [62] to compute the radial displacement of the capsule from the internal pressure. If on the other hand the capsule has a thin wall, strains can become large, and the linear elasticity hypothesis fails. For this case, in accordance with [9] the original young modulus is modified instead of employing finite elasticity theory. The nonlinear relationship in stress and strain (ϵ_{cap}) was phenomenologically characterized by [9]:

$$E_{cap} = E_{cap,0}(1 + a\epsilon_{cap}) \tag{27}$$

where ϵ_{cap} is the strain, $E_{cap,0}$ is the initial Young modulus at zero strain, and $a = 1.5$ to obtain an optimal fit with the experiment.

The capsules have an initial inner and outer radius $R_{in,0}$ and $R_{out,0}$ respectively, whereby the capsule thickness $H = R_{out,0} - R_{in,0} > 0.2R_{in,0}$ typically for thick capsules. The pressure difference along the capsule wall can be related to the change in radii by [9]:

$$p_{cap} = \frac{4}{3}E_{caps}\left(\frac{1}{1 - \Delta R_0^3/R_{out}^3} - 1\right)\frac{u(R_{out})}{R_{out}} \tag{28}$$

Where E_{caps} is the Young modulus of the capsule material, R_{out} is the outer radius, and $u(R_{out})$ is the displacement at the outer radius. The outer radius is related to the inner radius R_{in} by $\Delta R_0^3 = R_{out,0}^3 - R_{in,0}^3$ (incompressibility). To simulate the radius evolution of the capsule, one computes pressure p_{cap} by summing up all contact forces of the cells with the capsule, and divide this by the actual inner surface area. The radius from the nonlinear Eq. 28 could then be obtained using Newton's iteration method. This however, turned out not to be a good choice, as small fluctuations in the pressure causes cumbersome calculations. Instead, we update the radius using following ODE, formally similar to Eq. 12:

$$\frac{\gamma_{cap}}{R_{out}(t)}\frac{dR_{out}(t)}{dt} = p_{cap}(t) - \frac{4}{3}E_{caps}\left(\frac{1}{1 - \Delta R_0^3/R_{out}^3(t)} - 1\right)\frac{u(R_{out}(t))}{R_{0out}} \tag{29}$$

This ODE describes the radial expansion of capsule in time, using a lumped material damping parameter γ_{cap} which reflects the damping of the material. We assume that the capsule material damping does not influence the rather slow dynamics of the spheroid, so in practice γ_{cap} is chosen high enough to warrant numerical stability, but low enough to mimic the material' s low viscous resistance [48]. Using Eq. 29 results in a smooth evolution of the capsule radius.

4.5. Model setup and parameters

First, a single run is performed with a small clump of 10 cells all at the beginning of their cell cycle, to grow a spheroid up to the size of the capsule (just before point of confluence, (see Fig. 3b)). The cells grow until they reach a radius of $R_i = 7\,\mu$m. After each cell division, a new cell cycle time is assigned to each of the daughter cells, chosen randomly from a Gaussian distribution. The cell cycle time defines the intrinsic growth rate α_0. This configuration is then further used as starting configuration for all succeeding simulations. The model parameters for this initial configuration have been calibrated such that the area density, measured in a cryosection of width $10\,\mu$m of the resulting spheroid with $R = 100\,\mu$m, matches that of the experiments ($\sim 0.85\,/100\mu\text{m}^2$) [9]. For an overview of the model parameters, see Table 1.

From the data for the capsule radius at which the curve is in the transition stage T_1 to T_2 (Fig. 4, $t = 1d$) and using Eq. 28, we deduce a critical pressure $p_{crit} \sim 1500\,$Pa a which most of the bulk cells become necrotic. To express the cell variability in the cells' response on pressure we have generated a Gaussian distribution for this with mean 1500 Pa and standard deviation of 10 %.

The physical parameters responsible for the inter and intracellular friction are in the model represented by γ_{int}, $\gamma_{c,c,\perp}$, $\gamma_{c,c,||}$. Mechanical relaxation time of spheroids compressed over a longer time period indicate

relaxation times of 1 to 5 hours [47, 48]. We have calibrated these friction parameters in the model from a relaxation experiment starting from a compressed spheroid such that $T_{rel} \sim 2\,\mathrm{h}$ was obtained.

We ran for each parameter set one simulation i.e., a single realization of the stochastic growth process. We have verified that using different random seeds for the same parameter set has negligible influence on the simulation results (see section *Supplementary material*). This can be justified by observing that the growth process containing several thousands of cells, is self-averaging such that the variations on the level of individual cells cancel out at the population level.

A flow chart of the model algorithms is depicted in Fig. 14.

Parameter	**symbol**	**unit**	**value**	**ref**
Center Based Model -Capsule			$Model\ 0$ — $Model\ Ia$ —$Model\ Ib$	
Mean cell cycle time (*)	T_{cyc}	hours	17	[9]
Maximum cell radius	R_i	μm	14	observations
Cell Young's modulus (*)	E	Pa	400	[14]
Cell motility	D	m^2/s	10^{-16}	[17]
Adhesion energy	W	J/m^2	10^{-4}	[14]
Cell compressibility (*)	K	kPa	5 — $[2.5, 150]$, $K(\rho_{dm})$ — $K(\rho_{dm})$	[8, 33, 34]
Cell-cell friction $\|\|$	$\gamma_{c,c,\|\|}$	Ns/m^3	10^{10}	test runs
Cell-cell friction, $\perp$	$\gamma_{c,c,\perp}$	Ns/m^3	10^{10}	test runs
Cell-ECM friction,	γ_{ECM}	Ns/m^3	10^9	test runs
Cell-capsule friction	$\gamma_{c,cap}$	Ns/m^3	10^9	test runs
Cell relaxation time	T_{rel}	hours	2	[47, 48]
Stall growth rate	α_{qui}	-	No — No — 0.3	test runs
Hill exponent	n	-	No — No — 1	test runs
Hill threshold (*)	$\epsilon_{V_{tr}}$	-	No — No — 0.35	test runs
Cell lysis time (*)	T_{lys}	days	No — $[0.2, 14]$ — 6	test runs
Critical pressure bulk (necrosis) (*)	p_{crit}	kPa	1.5	observations
Critical rim thickness (necrosis)	λ_{crit}	μm	15	[9]
Cell solid mass fraction	ϕ	-	0.3	[22]
Center Based Model -Dextran			$Model\ II$	
Critical rim thickness (quiescence)	λ_{crit}	μm	30	test runs
Deformable Cell Model				
Cortex Young's modulus	E_{cor}	Pa	2400	[35]
Cortex thickness	h_{cor}	μm	0.1	[35]
Cell compressibility	K	Pa	5000	test runs
Capsule properties				
Young modulus	E_{cap}	kPa	68	[9]
Poisson ratio	ν_{cap}	-	0.5	[9]
Initial Radius	R_{in}	μm	100	[9]
Thickness (thin/thick)	H	μm	8/30	[9]

Table 1: Nominal physical parameter values for the model. An (*) denotes parameter variability meaning that the individual cell parameters are picked from a Gaussian distribution with $\pm 10\%$ on their mean value.

Acknowledgements

This work was supported by PhysCancer (France) and the EU 7th Framework Programme (Notox). P.N. acknowledges financial support from INCA (grant 2012-1-PL BIO-09-IO) and from the ANR Blanc SVSE5 Invaders. We would like to thank M. Delarue for his input. P.N. acknowledges F. Joanny and J. Prost for the useful discussions.

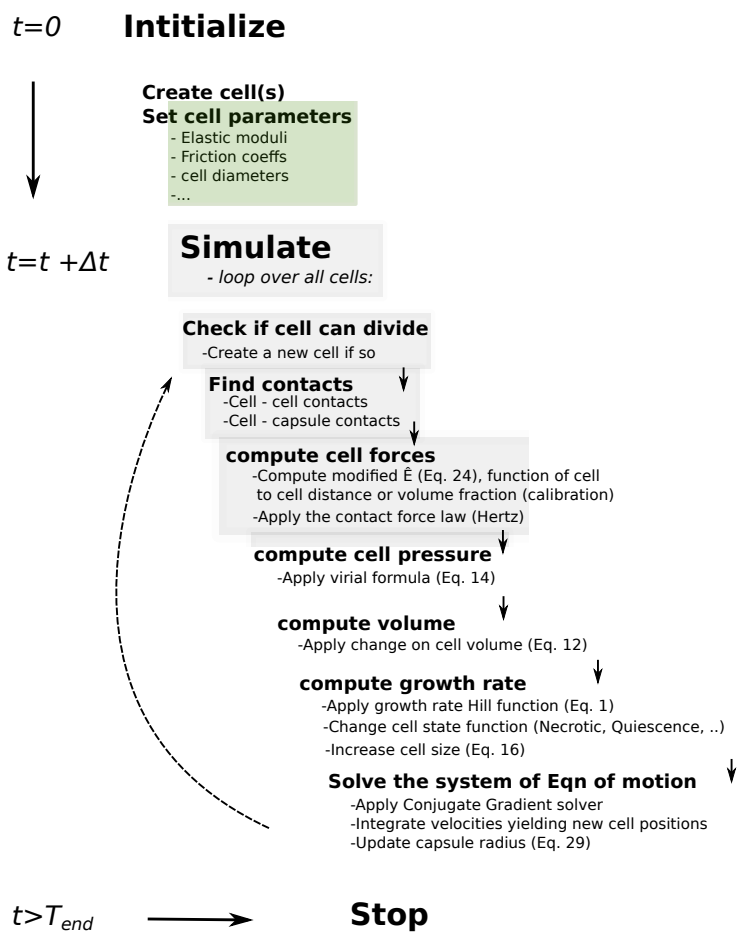

Figure 14: Model flow chart.

Competing interests

The authors have declared that no competing interests exist.

Supplementary material

Influence of cell cortex stiffness during compression

We considered whether the apparent boundary effect (E1.OIII) can be attributed purely to mechanical effects. For this, we used a spheroid compression experiment with a scaled capsule system using 400 (quiescent) DCM cells with different cortex properties (i.e. cells that have the original E_{cor} and cells with 10 times this value). It is shown in Fig. 15a that there can be a small mechanical effect in the case for a "high" stiffness of the cortex, as the simulations show that the cells near the boundary acquire higher pressures as compared to the bulk cells and a weak gradient from the center to the spheroid edge can be observed. This can be attributed to arching effects, the effect where layers of outer cells bears more stress compared to inner layers. The effect is higher for an increasing cortex stiffness. On the other hand, "softer" cells spread out more easily, diminishing the pressure differences. To investigate the boundary mechanics in a more realistic system with dividing cells, the DCM should extended with the capability to mimic mitosis. In our *simple* compression experiment with cells having estimated cortex properties, the boundary effect appears to be limited.

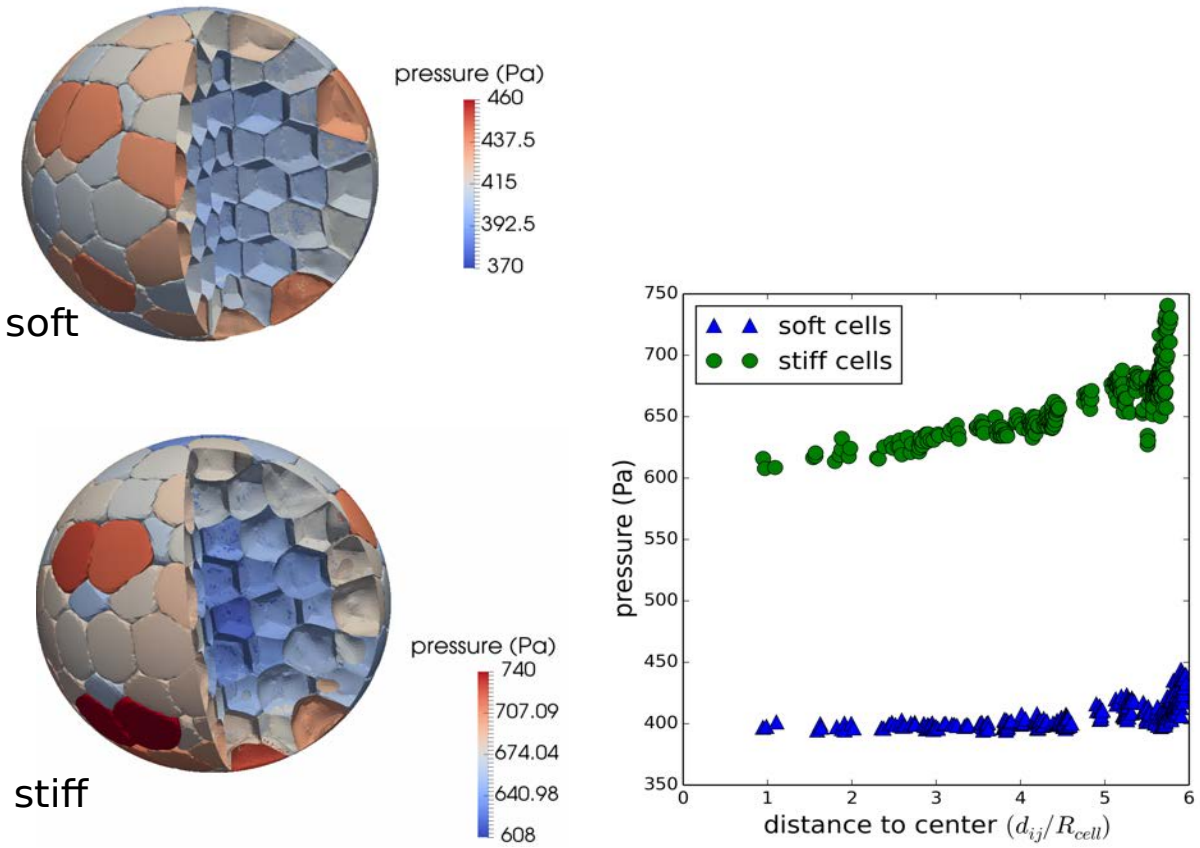

(a) (b)

Figure 15: (a) Simulation snapshots of DCM cells within a scaled capsule model, in case of "soft" (top) and "stiff" cells (bottom). (b) Internal cell pressure for deformable cells in a shrunk capsule for soft cells and stiff cells. The stiff cells show a higher variability in pressure as function of the distance to the capsule center. Notice that in the calibration simulations we use cells of equal volume prior to compression but the method can equally be applied to any prior volume distribution.

Comparison of "local" and "global" calibration methods

For the local calibration procedure, the constants $a_0 = 7 \times 10^3$, $a_1 = 3.5 \times 10^5$, $a_2 = -2.96 \times 10^7$, $a_3 = 2.068 \times 10^8$ and $a_4 = -1.515 \times 10^8$ in Eq. 25 yield a curve that matches well with the pressure - volume fraction curve obtained from the deformable cell simulations experiment (see Fig. 13). The function for $\tilde{E}(\tilde{d}_{ij})$ is monotonically increasing and shown in Fig. 16a (dashed line). The average for all cells during the simulation is given as well. A mentioned above, the resulting pressure - volume fraction curves are generally smoother compared to the one obtained from the local calibration. Friction parameters have less effect, as the calibration is based on a comparison of volume, rather than a cell to cell distance. As a test, we have compared the radial expansion curves for growth in the thin capsule using contact inhibited growth for both calibrations. As can be seen the difference between the two approaches is rather small, with a mutual variation of $5 - 7\%$.

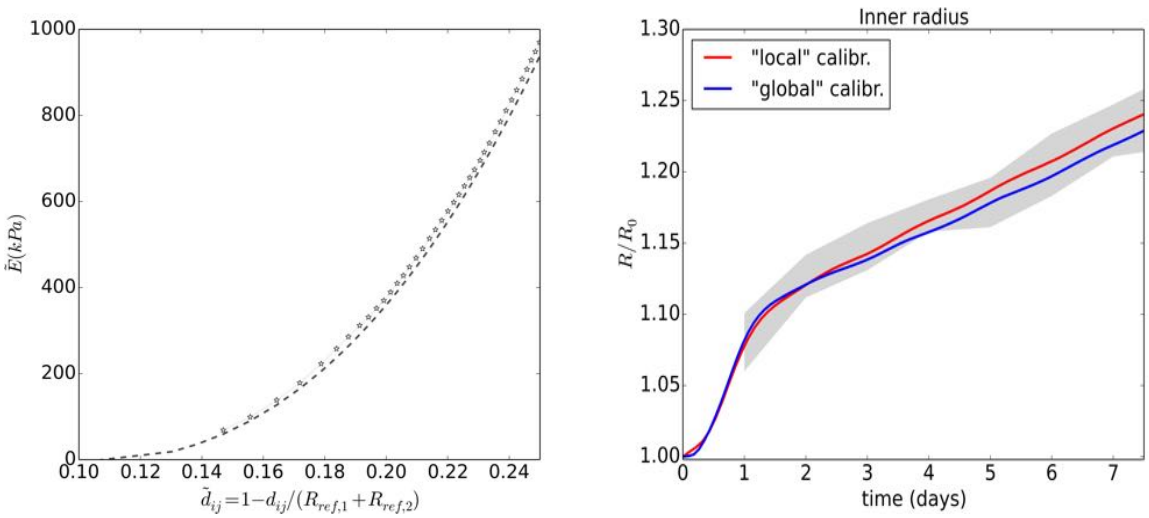

Figure 16: (a) Plot of the function $\tilde{E}(\tilde{d}_{ij})$ used for every cell (dashed line) and averages over all cells during a simulation (o-). (b) Comparison of the global an local calibration approach for a growing spheroid in the capsule with the proposed contact inhibition growth law.

Comparison of realizations with different random seedings

In analogy to experimental statistical procedures, we have performed different runs to test the effect of stochastic effects. Fig. 17 provides a direct comparison of the growth expansion in the thin capsule with the same parameters (optimal parameter set), using 4 different random seeds. Even after more than 7 days of simulation, little mutual differences can be observed, while the slopes of the curves are the same. This can be attributed to self-averaging effects such that the variations on the level of individual cells cancel out at the population level.

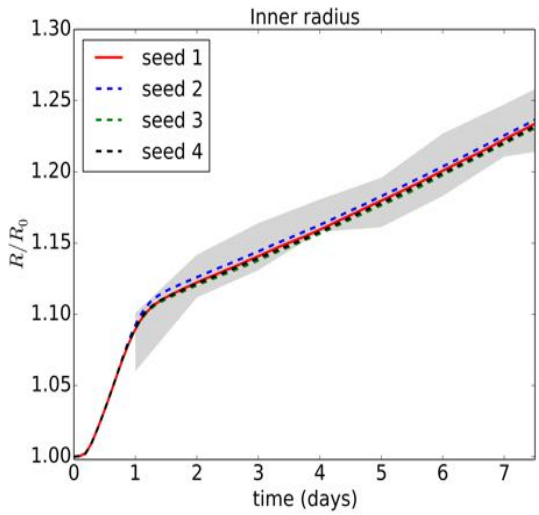

Figure 17: Thin capsule growth curves for four different realizations (seeds) of the stochastic processes in each of the cells using the same parameters.

Additional data

Experimental data and simulation data

New experimental raw data on the capsule can be found in the file **"capsule_dextran_data.xlsx"**. The data extracted from Alessandri et al. (2013) and Delarue et al. (2014) are in this file as well. The simulation data are in the file **"simulation_data.xlsx"** arranged by figure.

Videos

Video 1 (**CT26_free_growth.avi**) shows the simulated evolution of pressure a free growing CT26 spheroid. Note that a gradient in cell pressure gradually builds up from the center to the border of the spheroid.
Video 2 (**CT26_spheroid_capsule.avi**) shows the simulated evolution of pressure and cell volume of the CT26 spheroid growing in a thin capsule. The pressure increases gradually but remains approximately uniform over the spheroid.
Video 3 (**DCM_spheroid_compression.avi**) shows the simulation of a compression experiment of a spheroid in a capsule containing 400 deformable cells. Cell pressure and global volume fraction of the cell volume is indicated. The capsule radius shrinks gradually so that equilibrium pressures are measured. The cell pressure may be slightly higher at the spheroid border due to arching effects of the outer cells.

References

[1] A. J. Engler, S. Sen, H. L. Sweeney, and D. E. Discher, "Matrix Elasticity Directs Stem Cell Lineage Specification," *Cell*, vol. 126, pp. 677–689, 2006.

[2] D. T. Butcher, T. Alliston, and V. M. Weaver, "A tense situation: forcing tumour progression.," *Nature reviews. Cancer*, vol. 9, no. 2, pp. 108–22, 2009.

[3] M. Basan, T. Risler, J. F. Joanny, X. S. Garau, and J. Prost, "Homeostatic competition drives tumor growth and metastasis nucleation," *HFSP Journal*, vol. 3, no. 4, pp. 265–272, 2009.

[4] G. Helmlinger, P. A. Netti, H. C. Lichtenbeld, R. J. Melder, and R. K. Jain, "Solid stress inhibits the growth of multicellular tumor spheroids.," *Nature biotechnology*, vol. 15, pp. 778–83, aug 1997.

[5] G. Cheng, J. Tse, R. K. Jain, and L. L. Munn, "Micro-environmental mechanical stress controls tumor spheroid size and morphology by suppressing proliferation and inducing apoptosis in cancer cells.," *PloS one*, vol. 4, p. e4632, jan 2009.

[6] K. L. Mills, R. Kemkemer, S. Rudraraju, and K. Garikipati, "Elastic free energy drives the shape of prevascular solid tumors," *PLoS ONE*, vol. 9, no. 7, 2014.

[7] F. Montel, M. Delarue, J. Elgeti, L. Malaquin, M. Basan, T. Risler, B. Cabane, D. Vignjevic, J. Prost, G. Cappello, and J.-F. b. ç. Joanny, "Stress Clamp Experiments on Multicellular Tumor Spheroids," *Phys. Rev. Lett.*, vol. 107, p. 188102, oct 2011.

[8] M. Delarue, F. Montel, D. Vignjevic, J. Prost, J.-F. Joanny, and G. Cappello, "Compressive Stress Inhibits Proliferation in Tumor Spheroids through a Volume Limitation," *Biophysical Journal*, vol. 107, pp. 1821–1828, oct 2014.

[9] K. Alessandri, B. R. Sarangi, V. V. Gurchenkov, B. Sinha, T. R. Kießling, L. Fetler, F. Rico, S. Scheuring, C. Lamaze, A. Simon, S. Geraldo, D. Vignjevic, H. Doméjean, L. Rolland, A. Funfak, J. Bibette, N. Bremond, and P. Nassoy, "Cellular capsules as a tool for multicellular spheroid production and for investigating the mechanics of tumor progression in vitro.," *Proceedings of the National Academy of Sciences of the United States of America*, vol. 110, pp. 14843–8, sep 2013.

[10] D. Ambrosi and F. Mollica, "The role of stress in the growth of a multicell spheroid," *Journal of Mathematical Biology*, vol. 48, no. 5, pp. 477–499, 2004.

[11] H. B. Frieboes, F. Jin, Y.-L. Chuang, S. M. Wise, J. S. Lowengrub, and V. Cristini, "Three-dimensional multispecies nonlinear tumor growth-II: Tumor invasion and angiogenesis.," *Journal of theoretical biology*, vol. 264, pp. 1254–78, jun 2010.

[12] V. Cristini and J. Lowengrub, *Multiscale Modeling of Cancer: An Integrated Experimental and Mathematical Modeling Approach*. Cambridge University Press, 2010.

[13] D. Drasdo, R. Kree, and J. S. McCaskill, "Monte Carlo approach to tissue-cell populations," *Physical Review E*, vol. 52, pp. 6635–6657, dec 1995.

[14] S. Hoehme and D. Drasdo, "A single-cell-based model of tumor growth in vitro: monolayers and spheroids," *Physical Biology*, vol. 2, pp. 133–147, 2005.

[15] G. Schaller and M. Meyer-Hermann, "Multicellular tumor spheroid in an off-lattice Voronoi-Delaunay cell model," *Phys. Rev. E*, vol. 71, p. 51910, may 2005.

[16] A. Puliafito, L. Hufnagel, P. Neveu, S. Streichan, A. Sigal, D. K. Fygenson, and B. I. Shraiman, "Collective and single cell behavior in epithelial contact inhibition.," *Proceedings of the National Academy of Sciences of the United States of America*, vol. 109, pp. 739–44, jan 2012.

[17] D. Drasdo and S. Hoehme, "Modeling the impact of granular embedding media, and pulling versus pushing cells on growing cell clones," *New Journal of Physics*, vol. 14, no. 5, p. 55025, 2012.

[18] P. Van Liedekerke, M. M. Palm, N. Jagiella, and D. Drasdo, "Simulating tissue mechanics with agent-based models: concepts, perspectives and some novel results," *Computational Particle Mechanics*, vol. 2, pp. 401–444, nov 2015.

[19] D. Drasdo, S. Hoehme, and J. G. Hengstler, "How predictive quantitative modelling of tissue organisation can inform liver disease pathogenesis.," *Journal of hepatology*, vol. 61, pp. 951–6, oct 2014.

[20] S. HOEHME and D. DRASDO, "Biomechanical and Nutrient Controls in the Growth of Mammalian Cell Populations," *Mathematical Population Studies*, vol. 17, pp. 166–187, jul 2010.

[21] N. Jagiella, B. Müller, M. Müller, I. E. Vignon-Clementel, and D. Drasdo, "Inferring Growth Control Mechanisms in Growing Multi-cellular Spheroids of NSCLC Cells from Spatial-Temporal Image Data.," *PLoS computational biology*, vol. 12, p. e1004412, feb 2016.

[22] F. Feijó Delgado, N. Cermak, V. C. Hecht, S. Son, Y. Li, S. M. Knudsen, S. Olcum, J. M. Higgins, J. Chen, W. H. Grover, and S. R. Manalis, "Intracellular water exchange for measuring the dry mass, water mass and changes in chemical composition of living cells.," *PloS one*, vol. 8, p. e67590, jan 2013.

[23] T. P. Neufeld and B. A. Edgar, "Connections between growth and the cell cycle," *Current Opinion in Cell Biology*, vol. 10, pp. 784–790, 1998.

[24] A. Tzur, R. Kafri, V. S. LeBleu, G. Lahav, and M. W. Kirschner, "Cell Growth and Size Homeostasis in Proliferating Animal Cells," *Science*, vol. 325, no. 5937, pp. 167–171, 2009.

[25] M. Mir, Z. Wang, Z. Shen, M. Bednarz, R. Bashir, I. Golding, S. G. Prasanth, and G. Popescu, "Optical measurement of cycle-dependent cell growth," *Proceedings of the National Academy of Sciences*, 2011.

[26] R. Kafri, J. Levy, M. B. Ginzberg, S. Oh, G. Lahav, and M. W. Kirschner, "Dynamics extracted from fixed cells reveal feedback linking cell growth to cell cycle," *Nature*, vol. 494, no. 7438, pp. 480–483, 2013.

[27] B. Sinha, D. Köster, R. Ruez, P. Gonnord, M. Bastiani, D. Abankwa, R. V. Stan, G. Butler-Browne, B. Vedie, L. Johannes, N. Morone, R. G. Parton, G. Raposo, P. Sens, C. Lamaze, and P. Nassoy, "Cells respond to mechanical stress by rapid disassembly of caveolae," *Cell*, vol. 144, no. 3, pp. 402–413, 2011.

[28] B. I. Shraiman, "Mechanical feedback as a possible regulator of tissue growth.," *Proceedings of the National Academy of Sciences of the United States of America*, vol. 102, pp. 3318–3323, mar 2005.
[29] P. Mascheroni, C. Stigliano, M. Carfagna, D. P. Boso, L. Preziosi, P. Decuzzi, and B. A. Schrefler, "Predicting the growth of glioblastoma multiforme spheroids using a multiphase porous media model," 2016.
[30] D. O. Morgan, *The Cell Cycle: Principles of Control*. 2007.
[31] Y. Kim and H. G. Othmer, "A hybrid model of tumor-stromal interactions in breast cancer.," *Bulletin of mathematical biology*, vol. 75, pp. 1304–50, aug 2013.
[32] H. G. Othmer and Y. Kim, "Hybrid models of cell and tissue dynamics in tumor growth," *Mathematical Biosciences and Engineering*, vol. 12, no. 6, pp. 1141–1156, 2015.
[33] M. Delarue, J.-F. Joanny, F. Jülicher, and J. Prost, "Stress distributions and cell flows in a growing cell aggregate," *Interface focus*, vol. 4, no. 6, p. 20140033, 2014.
[34] L. Lin, A. Liu, Y. Yu, and C. Zhang, "Cell compressibility studies utilizing noncontact hydrostatic pressure measurements on single living cells in a microchamber," *Applied Physics . . .*, 2008.
[35] J.-Y. Tinevez, U. Schulze, G. Salbreux, J. Roensch, J.-F. Joanny, and E. Paluch, "Role of cortical tension in bleb growth.," *Proceedings of the National Academy of Sciences of the United States of America*, vol. 106, pp. 18581–6, nov 2009.
[36] D. Stamenovic and N. Wang, "Engineering approaches to cytoskeletal mechanics," *Journal of Applied Physiology*, vol. 89, pp. 2085–2090, 2000.
[37] D. Boal, *Mechanics of the Cell*. Cambridge University Press, 2 ed., 2012.
[38] M. Delarue, F. Montel, O. Caen, J. Elgeti, J.-M. Siaugue, D. Vignjevic, J. Prost, J.-F. b. ç. Joanny, and G. Cappello, "Mechanical Control of Cell flow in Multicellular Spheroids," *Phys. Rev. Lett.*, vol. 110, p. 138103, mar 2013.
[39] S. Hoehme and D. Drasdo, "Mathematical Population Studies : An International Journal of Mathematical Biomechanical and Nutrient Controls in the Growth of Mammalian Cell Populations," vol. 17, no. 166-187, pp. 37–41, 2010.
[40] Y. S. Chu, S. Dufour, J. P. Thiery, E. Perez, and F. Pincet, "Johnson-Kendall-Roberts Theory Applied to Living Cells," *Physical Review Letters*, vol. 94, no. 2, p. 28102, 2005.
[41] D. Drasdo, S. Hoehme, and M. Block, "On the Role of Physics in the Growth and Pattern Formation of Multi-Cellular Systems: What can we Learn from Individual-Cell Based Models," *Journal of Statistical Physics*, vol. 128, pp. 287–345, 2007.
[42] G. M. Odell, G. Oster, P. Alberch, and B. Burnside, "The mechanical basis of morphogenesis. I. Epithelial folding and invagination.," *Developmental biology*, vol. 85, no. 2, pp. 446–462, 1981.
[43] D. A. Beysens, G. Forgacs, and J. A. Glazier, "Cell sorting is analogous to phase ordering in fluids," *PNAS*, vol. 97, pp. 9467–9471, 2000.
[44] P. Van Liedekerke, B. Smeets, T. Odenthal, E. Tijskens, and H. Ramon, "Solving microscopic flow problems using Stokes equations in SPH," *Computer Physics Communications*, vol. 184, pp. 1686–1696, 2013.
[45] J. Galle, M. Loeffler, and D. Drasdo, "Modeling the effect of deregulated proliferation and apoptosis on the growth dynamics of epithelial cell populations in vitro," *Biophysical journal*, vol. 88, no. 1, pp. 62–75, 2005.
[46] F. Wottawah, S. Schinkinger, B. Lincoln, R. Ananthakrishnan, M. Romeyke, J. Guck, and J. Kas, "Optical Rheology of Biological Cells," *Phys. Rev. Lett.*, vol. 94, p. 98103, 2005.
[47] P. Marmottant, A. Mgharbel, J. Käfer, B. Audren, J.-P. Rieu, J.-C. Vial, B. van der Sanden, A. F. M. Marée, F. Graner, and H. Delanoë-Ayari, "The role of fluctuations and stress on the effective viscosity of cell aggregates.," *Proceedings of the National Academy of Sciences of the United States of America*, vol. 106, pp. 17271–5, oct 2009.
[48] *The Cellular Capsules technology And its applications to investigate model tumor*. PhD thesis, UPMC, 2013.
[49] J. H. Irving and J. G. Kirkwood, "The Statistical Mechanical Theory of Transport Processes. IV. The Equations of Hydrodynamics," *The Journal of Chemical Physics*, vol. 18, p. 817, jun 1950.
[50] P. Ghysels, G. Samaey, B. Tijskens, P. V. Liedekerke, H. Ramon, and D. Roose, "Multi-scale simulation of plant tissue deformation using a model for individual cell mechanics," *Physical Biology*, vol. 6, no. 1, p. 16009, 2009.
[51] P. Ghysels, G. Samaey, P. Van Liedekerke, E. Tijskens, H. Ramon, and D. Roose, "Multiscale modeling of viscoelastic plant tissue," *International Journal of Multiscale Computational Engineering*, vol. 8, no. 4, pp. 379–396, 2010.
[52] M. Basan, J. Prost, J.-F. Joanny, and J. Elgeti, "Dissipative particle dynamics simulations for biological tissues: rheology and competition.," *Physical biology*, vol. 8, p. 26014, apr 2011.
[53] P. V. Liedekerke, P. Ghysels, E. Tijskens, G. Samaey, B. Smeets, D. Roose, and H. Ramon, "A particle-based model to simulate the micromechanics of single-plant parenchyma cells and aggregates," *Physical Biology*, vol. 7, p. 26006, 2010.
[54] S. A. Sandersius, C. J. Weijer, and T. J. Newman, "Emergent cell and tissue dynamics from subcellular modeling of active biomechanical processes," *Physical Biology*, vol. 8, p. 45007, 2011.
[55] S. Tanaka, D. Sichau, and D. Iber, "LBIBCell: a cell-based simulation environment for morphogenetic problems," *Bioinformatics*, 2015.
[56] P. Van Liedekerke, E. Tijskens, H. Ramon, P. Ghysels, G. Samaey, and D. Roose, "Particle-based model to simulate the micromechanics of biological cells," *Physical Review E*, vol. 81, pp. 61906–61915, jun 2010.
[57] D. A. Fedosov, B. Caswell, and G. E. Karniadakis, "Systematic coarse-graining of spectrin-level red blood cell models," *Computer Methods in Applied Mechanics and Engineering*, vol. 199, no. 2932, pp. 1937–1948, 2010.
[58] J. C. Hansen, R. Skalak, S. Chien, and A. Hoger, "An elastic network model based on the structure of the red blood cell membrane skeleton.," *Biophysical journal*, vol. 70, pp. 146–66, jan 1996.
[59] T. Odenthal, B. Smeets, P. Van Liedekerke, E. Tijskens, H. Van Oosterwyck, and H. Ramon, "Analysis of Initial Cell Spreading Using Mechanistic Contact Formulations for a Deformable Cell Model," *PLoS Computational Biology*, vol. 9, p. e1003267, oct 2013.
[60] P. Pathmanathan, J. Cooper, A. Fletcher, G. Mirams, L. Montahan, P. Murray, J. Osborne, J. Pitt-Francis, A. Walter,

and S. J. Chapman, "A computational study of discrete mechanical tissue models," *Physical Biology*, vol. 6(3), p. 36001, 2009.

[61] R. Ananthakrishnan, J. Guck, F. Wottawah, S. Schinkinger, B. Lincoln, M. Romeyke, T. Moon, and J. Käs, "Quantifying the contribution of actin networks to the elastic strength of fibroblasts," *Journal of Theoretical Biology*, vol. 242, no. 2, pp. 502–516, 2006.

[62] L. D. Landau, L. P. Pitaevskii, E. M. Lifshitz, and A. M. Kosevich, *Theory of Elasticity, Third Edition: Volume 7 (Theoretical Physics)*. Butterworth-Heinemann, 1986.